



UNIVERSIDADE ESTADUAL DE CAMPINAS
SISTEMA DE BIBLIOTECAS DA UNICAMP
REPOSITÓRIO DA PRODUÇÃO CIENTÍFICA E INTELLECTUAL DA UNICAMP

Versão do arquivo anexado / Version of attached file:

Versão do Editor / Published Version

Mais informações no site da editora / Further information on publisher's website:

<https://academic.oup.com/jge/article/15/4/1561/5204267>

DOI: 10.1088/1742-2140/aab287

Direitos autorais / Publisher's copyright statement:

©2018 by Oxford University Press. All rights reserved.

DIRETORIA DE TRATAMENTO DA INFORMAÇÃO

Cidade Universitária Zeferino Vaz Barão Geraldo

CEP 13083-970 – Campinas SP

Fone: (19) 3521-6493

<http://www.repositorio.unicamp.br>

Analysis of time-lapse seismic and production data for reservoir model classification and assessment

Rafael Souza¹ , David Lumley^{1,2,4}, Jeffrey Shragge^{1,2,5},
Alessandra Davolio³ and Denis José Schiozer³

¹ Centre for Energy Geoscience, School of Earth Sciences, The University of Western Australia, Australia

² School of Physics and Astrophysics, The University of Western Australia, Australia

³ Faculty of Mechanical Engineering, University of Campinas, Brazil

⁴ Now at Department of Geosciences, University of Texas at Dallas, TX, United States of America

⁵ Now at Department of Geophysics, Colorado School of Mines, CO, United States of America

E-mail: rafael.medeirosdesouza@research.uwa.edu.au

Received 6 June 2017, revised 25 January 2018

Accepted for publication 27 February 2018

Published 9 May 2018



CrossMark

Abstract

The heterogeneous distribution of reservoir properties is one of the most important uncertainties in static and dynamic reservoir modelling. Petrophysical properties are usually interpolated within reservoir models from sparse well-log data, which can lead to highly uncertain estimates at inter-well locations that directly affect the reliability of fluid-flow model predictions of reservoir behaviour. To address this issue, one approach is to build an ensemble of equiprobable models that combine different geostatistical realisations of reservoir properties that ideally span the range of potential outcomes. While this process captures the impact of reservoir property distributions on the model response, a major challenge is classifying the subset of models in the ensemble best representing reservoir fluid-flow behaviour. Time-lapse seismic attributes are useful for reducing such uncertainties, since they image fluid-movement trends that provide insights regarding fault locations and distribution of reservoir properties, such as permeability and porosity. Accordingly, we introduce a methodology combining 4D seismic amplitude attributes and reservoir production data to classify fluid-flow models. This classification is based on applying thresholds for independent seismic and production objective functions. We develop and apply a new formulation of local dissimilarity maps to quantify differences between observed and modelled 4D seismic amplitudes. We test our methodology on the benchmark case UNISIM-I developed from observations from the Namorado Field, Campos Basin, Brazil. By comparing injection and production rates in relation to 4D seismic amplitude trends within each region, we identify nine models out of an ensemble of 100 that are judged optimal via the required seismic and production objective function thresholds. Thus, we obtain an improved quantitative evaluation of the impact of reservoir production on the 4D seismic signal. Combining seismic and production data offers interpretation scenarios that automatically identify realistic fluid-flow models that would be helpful for updating reservoir properties.

Keywords: fluid-flow model, time-lapse (4D) seismic, ensemble of models, history matching, model selection, reservoir property update

(Some figures may appear in colour only in the online journal)

1. Introduction

Fluid-flow models have long been used to assist in reservoir development and management activities (Aziz and Settari 1979, Oliver *et al* 2008, Oliver and Chen 2011, Schiozer *et al* 2015). These models simulate the dynamics of fluid flow in porous media, which is used to predict future hydrocarbon reservoir behaviour. Flow models have been developed based on a wide range of different data sources including well logs, field seismic data and laboratory measurements of rock and fluid properties (Fanchi 2006). However, because each data source has its own characteristic scale length, horizontal and vertical resolution and areal coverage, it is unlikely that a single fluid-flow model will adequately capture the heterogeneity of reservoir properties. One key fluid-flow model building challenge is reliably extrapolating information derived from geographically sparse well logs to provide estimates of porosity and permeability distributions throughout a reservoir. Accordingly, in static and dynamic reservoir modelling, property heterogeneity is a source of errors, such as the number, locations and hydraulic properties of faults, which altogether can lead to highly uncertain production forecasts.

Even though uncertain production forecasts increase reservoir management risks, deterministic approaches using a single model are often the initial (and final) choice for static and dynamic reservoir modelling. Deterministic approaches cannot capture the full range of expected reservoir response to development activity as they do not account for the significant uncertainties associated with reservoir property heterogeneity. To examine the impact of reservoir property heterogeneity, one increasingly common strategy is to follow a stochastic approach and build an ensemble of equiprobable models that combine different geostatistical realisations of reservoir properties that ideally span the range of potential outcomes (Doyen 2007, Schiozer *et al* 2017). By sampling the parameter space one can generate posterior statistics that help quantify uncertainties on the model response due to variable reservoir property realisations, which provides invaluable information for reservoir development and management engineers (Mesquita *et al* 2015). However, a major challenge with this approach is selecting the subset of stochastic models that optimally represent reservoir behaviour. Effectively and efficiently addressing this issue requires developing an automated assessment procedure for identifying and classifying fluid-flow models that are both physically realisable and consistent with all available geophysical, production and geological data.

Current model classification procedures typically use criteria based on a combination of production data, such as bottom-hole pressure, water production rates and water cut values (Avansi and Schiozer 2015a, Maschio and Schiozer 2016). While this approach can identify models that reasonably reconstruct production history, the absence of geological information poses a challenge for identifying models consistent with the observed geological settings. In addition, inferring distributions of reservoir properties remains highly uncertain where no 4D seismic attributes are available to

indicate fluid-movement trends (Lumley 1995b, Lumley and Behrens 1998, Kjelstadli *et al* 2005, Ullmann *et al* 2011, Barkved 2012). This suggests that incorporating additional information obtained from 4D seismic data, where present, should improve the model classification process.

Incorporating seismic data in a quantitative manner requires transforming the information content into a format compatible with fluid-flow modelling outputs. One of the main associated challenges is that 4D seismic amplitude information exists in volumes acquired at a few sparse points in calendar time, which is in contrast to the relatively continuous production time-series data. A number of approaches extract, filter and segment 4D seismic attribute maps to quantify time-lapse reservoir changes (Tillier and Veiga 2012, Derfoul *et al* 2012). These methods binarize 4D attribute maps to calculate a local modified Hausdorff distance quantifying the (dis)similarity of two images (e.g. modelled and observed 4D seismic amplitude maps). Tillier and Veiga (2012) successfully apply this method in a synthetic steam-assisted gravity drainage production scenario, and improve objective function convergence in a history matching (HM) procedure when compared to a conventional least-squares optimisation approach (Gosselin *et al* 2003). Obidegwu (2015) compares binary images from saturation maps extracted from fluid-flow models directly with their binary seismic counterparts, which leads to the binary inversion domain being a 'quick-look alternative' for reservoir management. However, these approaches neither account for rock physics nor seismic forward modelling constraints, and thus neglect the influence that subsurface properties (e.g. rock bulk modulus) and acquisition parameters (e.g. seismic wavelet) have on the seismic amplitude response. This leads to an inconsistency between the mathematical model and observed physical system that may decrease the reliability of model predictions.

The goal of our study is to define quantitative criteria for use in classifying fluid-flow models from an ensemble of equiprobable realisations, according to their consistency with both 4D seismic amplitude maps and production data. Our approach accepts (or rejects) models based on acceptance thresholds defined independently for seismic and production objective functions. For our seismic objective function, we reformulate the binarisation method developed by Tillier *et al* (2012) introducing a new 'informative' local dissimilarity map (ILDm) that identifies the source of the differences (e.g. observed or modelled seismic data). We define our production objective function following the normalised quadratic deviation with signal (NQDS) approach (Avansi *et al* 2016). Thus, the suite of models that optimally satisfy both objective functions are likely to be those most consistent with the available geological, geophysical and engineering data, and thereby offer the most physically consistent insights into fluid-flow, porosity and permeability distributions as well as fault locations and fluid-flow characteristics.

This manuscript begins by exploring the role of production objective functions on fluid-flow model calibration and their integration with 4D seismic amplitudes for monitoring purposes. We discuss seismic forward modelling

based on the zero-offset seismic amplitude response of fluid-flow models, and specifically discuss how to effectively compare synthetics and reference 4D seismic data attributes. After formulating our seismic and production objective functions, we define the quantitative acceptance threshold criteria used for model selection. We then apply these principles in a synthetic 4D case study based on a benchmark fluid-flow model built on observations from the Namorado Field in Campos Basin, Brazil (Avansi *et al* 2016). We conclude with a discussion on the implications of these results for integrating 4D seismic attributes into workflows aiming to estimate and/or update reservoir properties and structural features for fluid-flow modelling, and their potential benefits for the monitoring and optimal recovery of hydrocarbon reservoirs.

2. Seismic objective function

The heterogeneous distribution of reservoir properties is one of the most significant uncertainties in static and dynamic reservoir modelling (Lumley 2006, Doyen 2007). Thus, accurately calibrating these reservoir properties within fluid-flow models is mandatory for predictive reliability (Oliver and Chen 2011, Schiozer *et al* 2015). Procedures for the updating of reservoir properties within fluid-flow models (e.g. HM) often use numerical optimisation approaches (i.e., gradient-based) that aim to minimise a production objective function (OF_p) defined as the mismatch (e.g. L_2 norm) between forward modelled and observed production data (Gomez *et al* 1999, Oliver and Chen 2011). While there are many successful HM cases (Oliver and Chen 2011, Bertolini and Schiozer 2011), solely examining production data does not allow the use of important spatial information derived from 4D seismic data. In particular, because subsurface fluid changes are commonly observable in 4D seismic attribute maps, these maps are useful for assessing a fluid-flow model's ability to predict 4D seismic observations. While extending the HM procedure to directly include 4D seismic data within a joint global inversion strategy represents an ideal goal, a number of studies suggest that following this approach can lead to unstable inversion procedures (Gosselin *et al* 2003, Roggero *et al* 2007). This observation motivates us to develop an alternative approach based on an independent seismic objective function (OF_s) that, when used in conjunction with a production objective function OF_p , is useful for fluid-flow model assessment and, potentially, for inclusion in model updating workflows.

Developing an effective OF_s requires recognising and accounting for a key difference between seismic amplitude maps (or volumes) and production data: the former typically consist of millions of pixels (billions of voxels), while the latter comprise hundreds of values. A typical HM analysis uses production data in a least-squares optimisation procedure to estimate reservoir properties such as porosity and permeability at each model grid cell. However, an HM procedure is unlikely to converge due to the lack of sensitivity of global objective functions to differences between

synthetic and observed 4D seismic amplitude calculated at each pixel (or voxel). Moreover, the high computational demand of fluid-flow simulations limits the number of parameters in HM procedures. Therefore, the goal of seismic HM should not be to accurately recover each pixel's value; rather, it should aim to capture the main fluid-flow features such as high-permeability channels, flow barriers and fault locations that offer the greatest influence on fluid-flow patterns (Lumley and Behrens 1998, Calvert 2005, Tillier and Veiga 2012).

We develop a procedure for calculating an OF_s that is based on image binarisation and dissimilarity assessment. This procedure allows us to locally highlight main fluid-flow reservoir features in the seismic data (e.g. high-permeability channels and faults) to assist with interpreting the effects of hydrocarbon production on observed 4D seismic amplitudes.

2.1. Image binarisation and similarity

One strategy for developing an OF_s is to adapt image analysis techniques that locate and quantify the (dis)similarities between any two given images (here the synthetic and observed 4D seismic attribute maps). One candidate approach is to apply a Hausdorff distance (HD) measure (Matheron 1975, Huttenlocher *et al* 1993), which is an established image comparison metric. In practice, though, the HD metric is very sensitive to outlier pixels, which means that isolated small image artefacts might significantly affect this measure. It is also not well adapted to noisy images (Tillier and Veiga 2012). In this case, the HD represents a global measure that cannot highlight local dissimilarities. Baudrier *et al* (2008) address the issue of the local distance by introducing the local dissimilarity map (LDM) measure between any two images. This approach uses a sliding window to calculate the local dissimilarity at any given pixel using a modified HD measure between two sub-images within the local window centred at that pixel. This definition both handles empty point sets and permits tuning of the sliding window parameters to more efficiently capture local dissimilarity.

The first step in estimating an LDM is to cluster the information contained in 4D seismic attribute maps into binary groups by applying a k -means++ algorithm (Arthur and Vassilvitskii 2007). The k -means++ algorithm chooses the clusters centroids and estimates a distance transform (DT) map that measures the discrepancy between each point in the map in relation to each centroid. We use the squared Euclidean distance to define the DT between the pixel value at x_m and that at the cluster centroid c_j :

$$DT(x_m, c_j) = (x_m - c_j)^2, \quad (1)$$

where $m = 1, N$ data points (or pixels) in the image and $j = 1, K$ are the number clusters. Note that DT is a measure of how far the amplitude value at the x_m location is from that at the centroid c_j . Other metrics (e.g. Hamming distance or current measurement) may also be applicable (Obidegwu 2015). In this context, Tillier *et al* (2012) defines the LDM

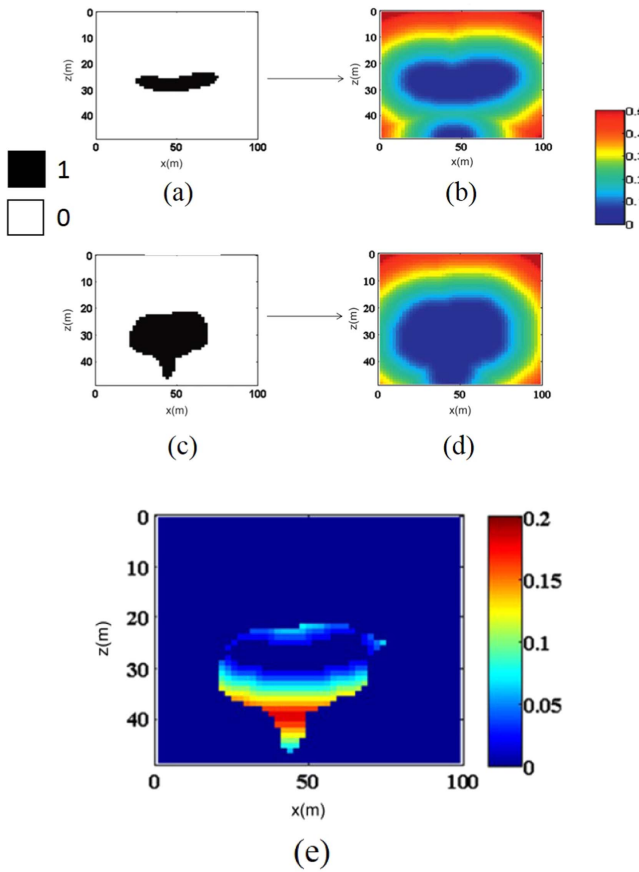


Figure 1. Illustration of Euclidean DT: (a) binary image A ; (b) image A distance transform A_c ; (c) binary image B ; (d) image B DT B_c ; and (e) images A and B LDM from equation (3) and the respective LDM objective function from equation (5). Adapted from Tillier et al (2012).

between two images $A = A(x_m)$ and $B = B(x_m)$ as

$$LDM(A, B, c_j) = |A_c - B_c| \max(DT(A, c_j), DT(B, c_j)), \tag{2}$$

where $A_c = A_c(x_m)$ and $B_c = B_c(x_m)$ are the clustered images of A and B , respectively. Figure 1 illustrates the LDM concept. Let images A_c and B_c (figures 1(a)–(c)) represent clustered baseline and monitor seismic attributes, respectively. In these maps, we associate locations exhibiting a 4D signal with values of one (black pixels) and those without with zeros (white pixels). Figures 1(b)–(d) show the calculated $DT(A, c_j)$ and $DT(B, c_j)$ maps, respectively, while figure 1(e) presents the associated $LDM(A, B, c_j)$. The LDM is zero for pixels where the two images are equal and is otherwise equal to the maximum distance value as per equation (2). We note that the LDM highlights the local dissimilarities between these two images, and thus offers a quantitative alternative for comparing 4D seismic attribute maps. However, they neither identify the image from which any dissimilarities arise nor do they differentiate between areas with no 4D signal from those

with an equal 4D signal. We address these issues in the following section.

2.2. Informative image binarisation and dissimilarity for fluid-flow applications

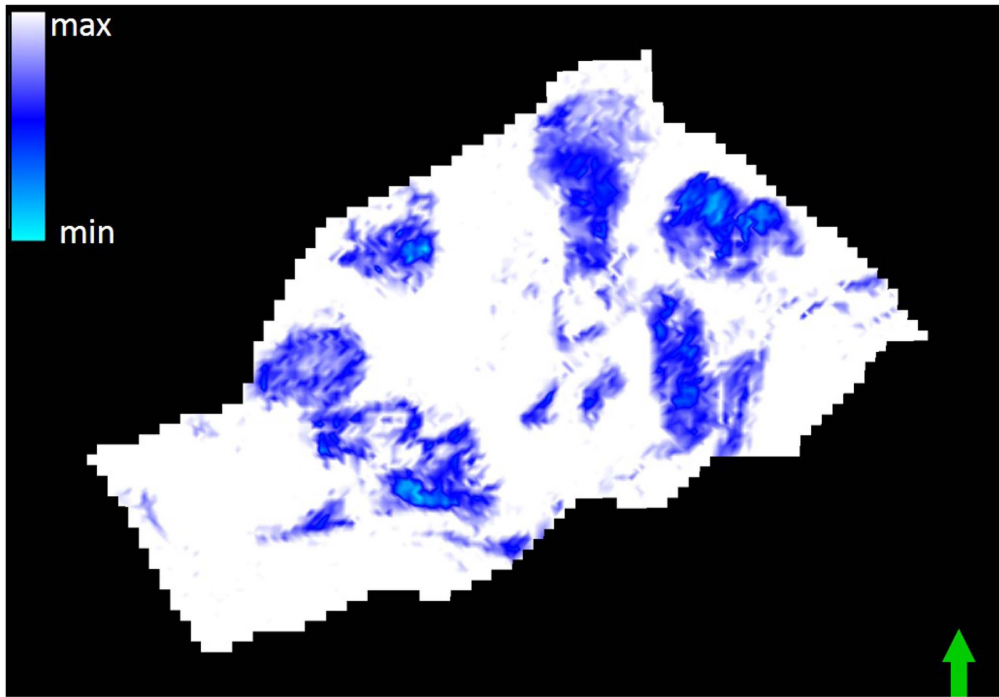
The example presented in figure 1 suggests that the LDM approach can provide a quantitative comparison between observed and synthetic 4D seismic amplitude maps. Conceptually speaking, the observations highlighted in figure 1 can be replicated by applying a coupled four-step seismic-reservoir modelling procedure: (1) develop a physical model of reservoir and elastic properties; (2) use a fluid-flow modelling engine to simulate the dynamic reservoir response over the selected period of time; (3) apply a seismic modelling procedure to generate the baseline and monitor synthetic seismic data sets, extract seismic attribute maps from each survey, and derive the 4D seismic amplitude change map; and (4) estimate the LDM for analysis purposes.

Figure 2 presents a reservoir scenario that highlights injection activities. Figure 2(a) presents a map of the reference 4D seismic amplitude changes where negative values indicate stiffening of the porous rock due to increased water saturation. We apply the k -means++ algorithm to cluster information in figure 2(a) into two clusters to form the binarised map B_c shown in figure 2(b). Blue (white) values indicate a presence (absence) of 4D seismic signal. Figure 3(a) shows the noise-free synthetic 4D seismic amplitude map A resulting from the 1D convolution between the 50 Hz Ricker wavelet and the reflection coefficient (RC) extracted from the fluid-flow model, which resembles the main observed 4D amplitude trends when compared to figure 2(a). Figure 3(b) presents the clustered map A_c of A (figure 3(a)) that similarly shows the presence (orange) or the absence (white) of 4D signal. Figure 4(a) superimposes the clustered images extracted from the maps of modelled (A_c in orange) and observed (B_c in blue) 4D amplitude changes from figures 2(a) and 3(a), which allows us to identify locations where the model and observations (dis)agree.

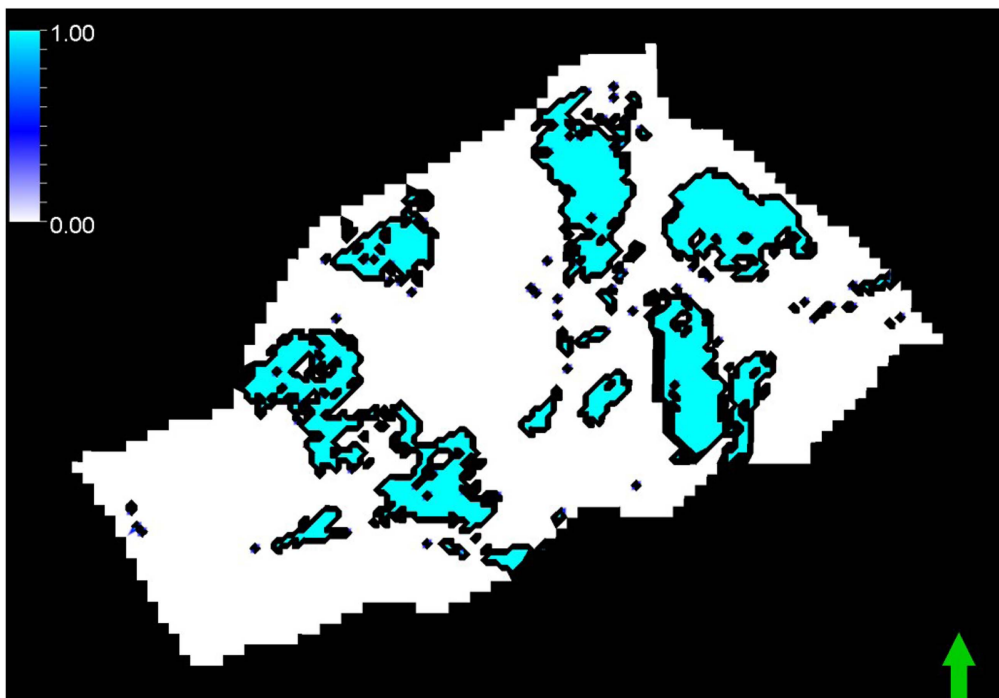
To quantify this degree of local (dis)similarity, we adapt the DT measure in equation (1) of the observed and synthetic clustered maps (figures 2(b) and 4(b)), respectively) to define a new 4D ILDM measure for each pixel:

$$IDLM(A, B) = \begin{cases} (A_c - B_c) \left| \frac{DT(A, c_j)}{\max(DT(A, c_j))} \right| & \text{if } A_c > B_c, \\ (A_c - B_c) \left| \frac{DT(B, c_j)}{\max(DT(B, c_j))} \right| & \text{otherwise.} \end{cases} \tag{3}$$

Note that the ILDM in equation (3) both identifies the map containing the more significant information and assigns a scaled single value to each pixel. Identical pixels have zero ILDM values, while non-zero values quantify the (dis)



(a)



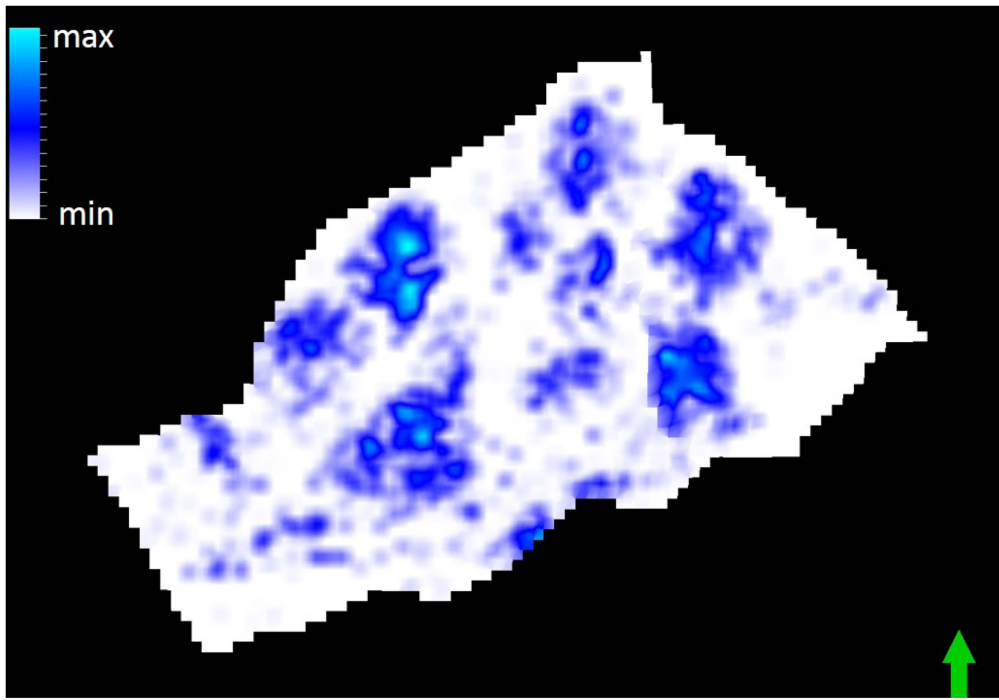
(b)

Figure 2. Illustration of: (a) observed 4D seismic amplitude changes; and (b) binary 4D seismic amplitude map where the 4D seismic signal is highlighted by the blue clusters, and the background information (i.e. no 4D changes) is shown in white.

similarity between two clustered maps. The upper (lower) expression is applied if the dissimilarity information comes from map A_c (B_c). Figure 4(b) presents the 4D ILDM for the modelled and observed 4D amplitude maps, A and B , respectively. In this case, positive values (red) indicate that

information comes from the simulation data, while negative (blue) indicates information from the observed 4D seismic data.

To associate a quantitative indicator of data mismatch for each simulation model, we define our seismic objective



(a)



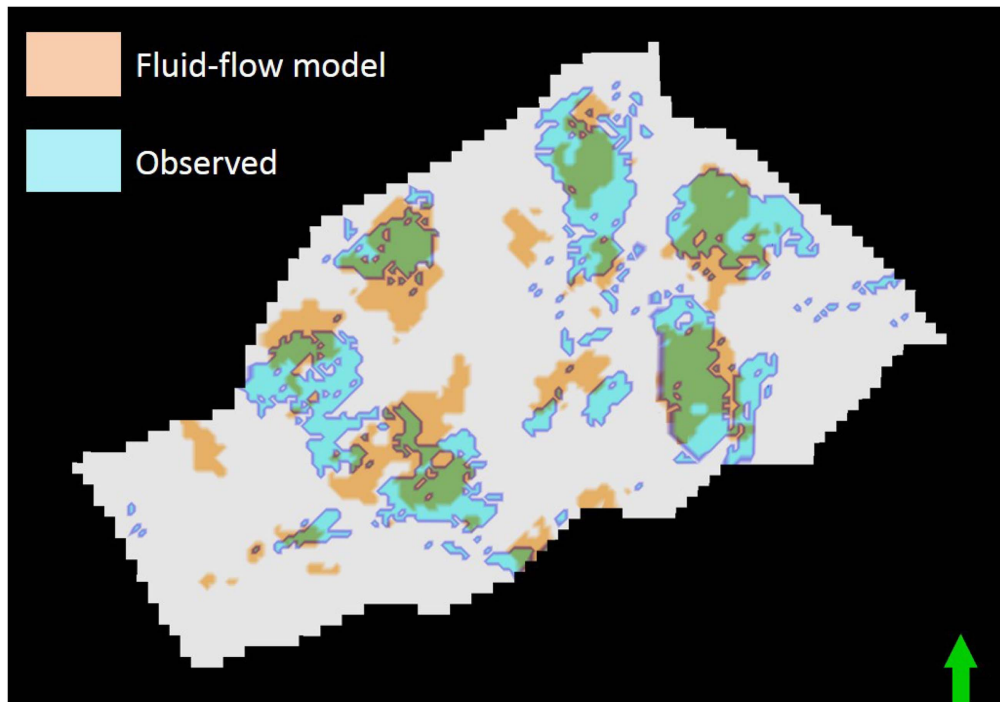
(b)

Figure 3. (a) Synthetic 4D amplitude changes in map A computed from a fluid-flow model. (b) Clustered map A_C of the map in (a), where the presence and absence of 4D signal is indicated by orange and white pixels, respectively.

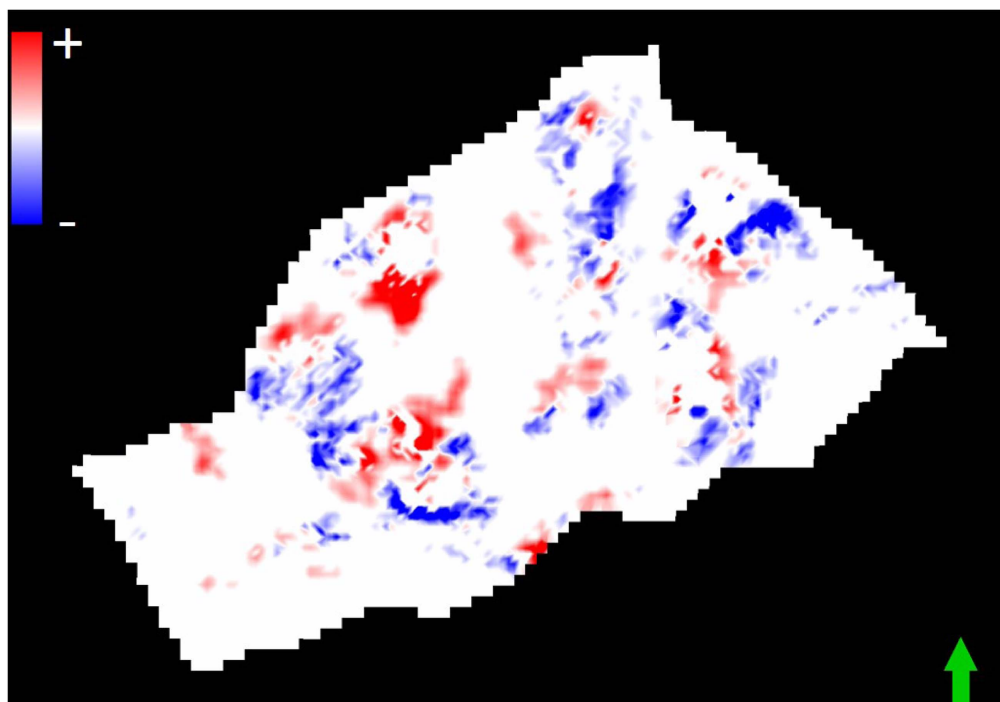
function OF_S as:

$$OF_S = \frac{\|ILDM(A, B)\|_2}{\max(\|DT(A)\|_2, \|DT(B)\|_2)}, \quad (4)$$

where $\|\cdot\|_2$ indicates an L_2 norm and OF_S is normalised to fall within $0 \leq OF_S \leq 1$. Low (high) OF_S values indicate that images A and B are more (dis)similar.



(a)



(b)

Figure 4. (a) Superimposition of the clustered maps of the modelled (orange) and observed (blue) 4D amplitude changes. (b) Respective ILDM defined in equation (3). Note that the ILDM highlights the dissimilarities between observed and synthetic 4D seismic amplitude maps in figures 2(a) and (b).

3. Methodology

This section develops our methodology for classifying a suite of earth models from an ensemble that is internally consistent with

both seismic and production data. We define consistency as satisfying independent acceptance thresholds for both seismic and production objective functions, T_S and T_P , respectively. We divide our methodology into four steps, which we illustrate in

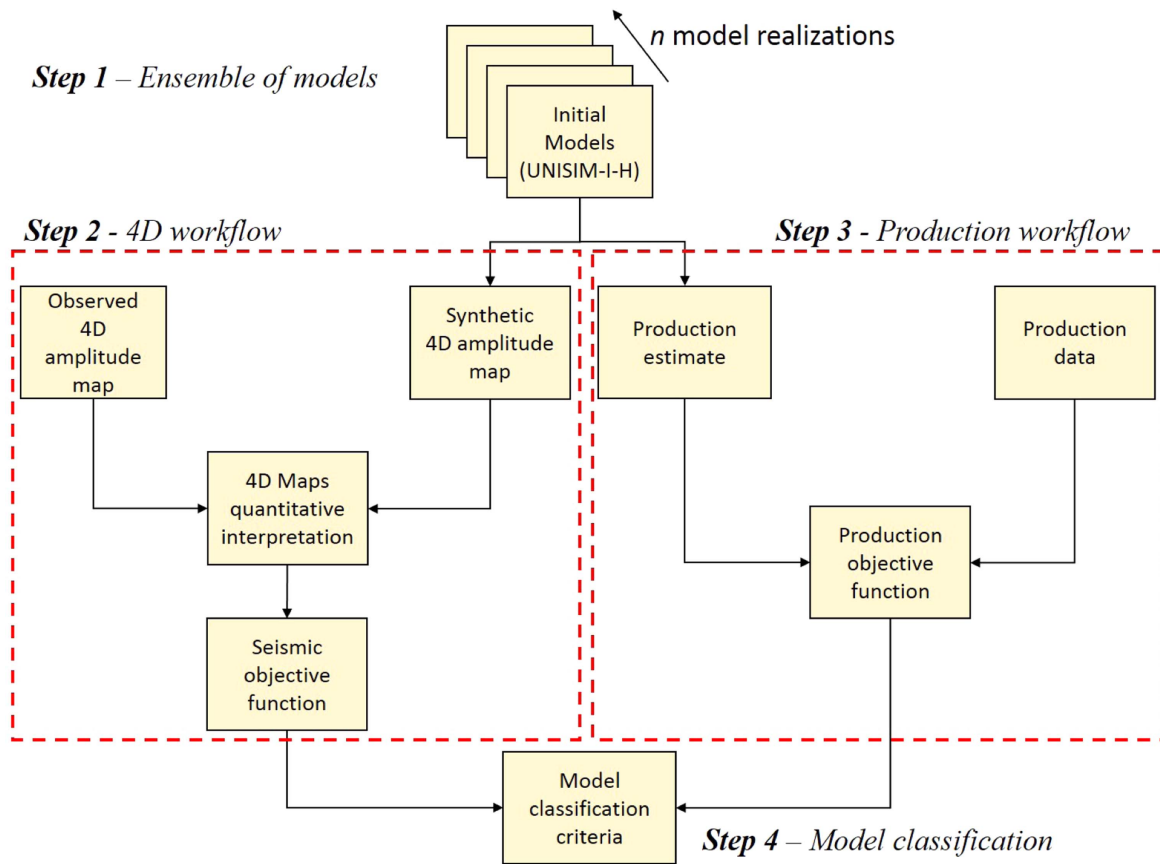


Figure 5. Workflow steps to define the model selection criteria. Step 1 generates the ensemble of models. Step 2 involves seismic forward modelling and interpreting the 4D amplitude changes maps and evaluating the seismic objective function OF_S . Step 3 estimates the production objective function (OF_P). Step 4 selects the optimal models by applying our criteria to the OF_S and OF_P .

figure 5: (1) generate an ensemble of equiprobable fluid-flow models; (2) apply a 4D seismic workflow; (3) apply a production modelling workflow; and (4) assert the model classification routine. We discuss each step below.

3.1. Step 1: ensemble of models

The first step is to define an ensemble of fluid-flow models to be used as input to the ensuing procedural steps. As our methodology focuses on model classification and not on model development, we assume that a suitable model ensemble already exists that possesses representative characteristics aligned with the aims of the study. For instance, in this study we opt for an ensemble of equiprobable models that capture reservoir property heterogeneity by combining different geostatistical realisations that ideally span the range of potential reservoir responses. Accordingly, this ensemble collectively captures the uncertainty estimates associated with the reservoir model predictions. The generation of a representative ensemble of Earth models used in our example is detailed in Schiozer et al (2017) and Avansi et al (2016).

3.2. Step 2: 4D seismic modelling workflow

In this step, we forward the seismic model the synthetic seismic amplitude response of all models in the ensemble using the procedure discussed in section 5 below. We assume

that the seismic data image polarity is equivalent to a zero-phase wavelet, and use a convention where positive values correspond to positive reflectivity and 4D differences are defined as the monitor minus the baseline seismic survey data (Lumley 1995a, 2001). We then extract rms maps of the observed and synthetic 4D seismic amplitude in order to apply the ILDM (equation (3)) for calculating the seismic objective function (equation (4)). The map extraction procedure is defined on a case-by-case basis; therefore, we describe our specific example in section 5 below. Note that the optimal domain for the integration of production and seismic data (e.g. seismic amplitudes or impedances) needs to be determined on a case-by-case basis. In this study, we identify production induction 4D seismic amplitude differences in the maps. Our choice of domain builds upon previous research that quantitatively confirms that the uncertainties associated with seismic amplitude changes are lower than those of the seismic impedances due to the combined impact of seismic noise and the instability of the seismic inversion procedures. We also observe an uncertainty increase proportional to the seismic data signal-to-noise levels (Souza et al 2017).

3.3. Step 3: production workflow

To quantify the mismatch between the reference (historical) and simulated production data at time t_i (obs_i and sim_i ,

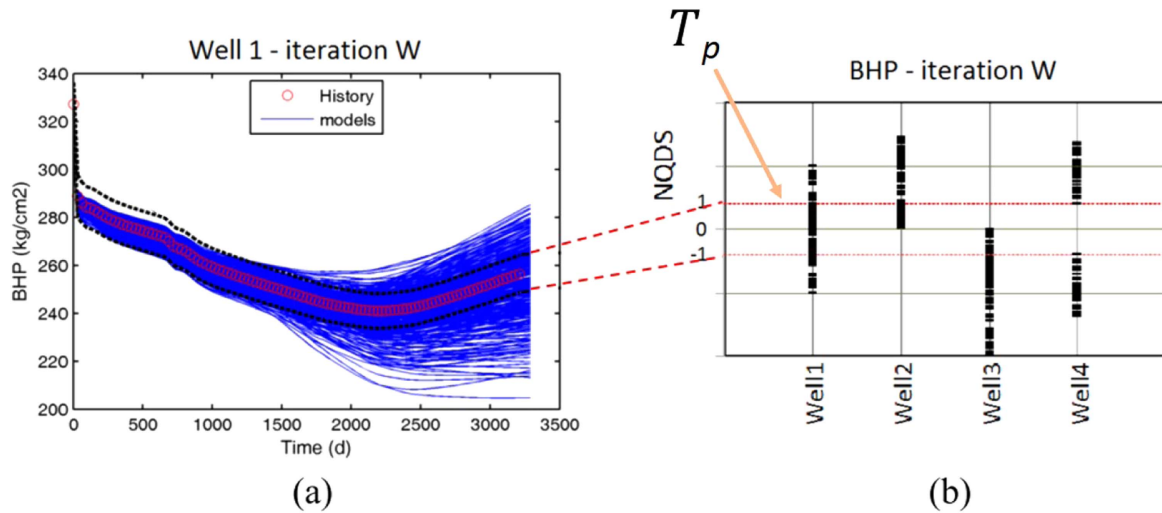


Figure 6. Assessment of production data: (a) time-varying bottom-hole pressure and an associated production acceptance threshold T_p ; (b) OF_P per well indicating the range of acceptable values (dashed line in red).

respectively), we use a production objective function, OF_P , that is based on the NQDS approach (Avansi et al 2016):

$$OF_P \equiv |NQDS(obs_i, sim_i)| = \left| \frac{QDS(obs_i, sim_i)}{AQD(obs_i)} \right|, \quad (5)$$

where $|\cdot|$ is absolute value, QDS is the quadratic deviation with signal,

$$QDS(obs_i, sim_i) = \frac{SD}{|SD|} \|obs_i - sim_i\|_2, \quad (6)$$

SD is the simple deviation,

$$SD(obs_i, sim_i) = \sum_{i=1}^{N_i} (obs_i - sim_i), \quad (7)$$

and AQD is the acceptable quadratic deviation

$$AQD(obs_i) = \|obs_i \gamma + \epsilon\|_2, \quad (8)$$

where γ is a user-defined positive-valued acceptance criterion (percentage) for each data series, and ϵ is a small positive constant to avoid division by zero. The NQDS value indicates the quality of the match between observed and simulated production data and its absolute value can be used to define a production selection criteria in Step 4 below. Note that because we define and apply OF_P independently of OF_S there is no need to cross-normalise this function.

3.4. Step 4: model classification

The final step combines the measures calculated in Steps 2 and 3 to classify the models in the ensemble. We define our model classification criterion by applying independent seismic and production acceptance thresholds, T_S and T_P on OF_S and OF_P defined in equations (4) and (5), respectively. The value of each acceptance threshold is determined on a case-by-case basis (see section 5). These criteria allow us to identify models with an acceptable match between seismic and production data that satisfy both $OF_S < T_S$ and $OF_P < T_P$. Figures 6(a) and (b) illustrate how T_P is

applied to OF_P values (i.e. prior to applying the absolute value operator in equation (5)), respectively. We consider acceptable any given model that has OF_P values within $0 \leq |NQDS| \leq T_p$.

3.5. Model classification

To facilitate understanding of our model classification procedure, we introduce four model classes: (1) Type 1 models that satisfy both seismic and production data according to our defined criteria ($OF_S < T_S$ and $OF_P < T_P$); (2) Type 2 models that are acceptable by seismic constraints, but are rejected by production data ($OF_S < T_S$ and $OF_P > T_P$); (3) Type 3 models that are rejected by seismic data, but are acceptable by production data constraints ($OF_S > T_S$ and $OF_P < T_P$); and (4) Type 4 models are rejected by both seismic and production data ($OF_S > T_S$ and $OF_P > T_P$). Models falling in each type are important as they offer a different perspective of the results. For example, Type 2 models could suggest an unconsidered interpretation hypothesis that may be overlooked due to rejection based on production data. Similarly, a better correlation with the 4D seismic amplitude map may indicate that away from the wells, the property distribution (e.g. porosity and permeability) is closer to the true model than a model selected by the production data alone. Similar understandings arise when interpreting Types 3 and 4.

Note also that the goal of our method is to classify reservoir models based on the dual objectives of fitting both production and seismic data. Once we classify the models, they can be further refined by applying practical business decision methods. For instance, we could select from our Type 1 range three reservoir models based on their occurrence probability (e.g. P10/P50/P90) (Schiozer et al 2004, Meira et al 2016). We could also select model Types 1–3 and discard the Type 4 model (i.e. poor fit to both production and seismic criteria). In fact, our method provides more choices

and information of how to select/subsample model space than just P10/P50/P90.

4. Data set description

This section provides an overview of the UNISIM-I benchmark model (Maschio *et al* 2015) that we use to validate our methodology. We outline the methodology used to generate the initial ensemble of models. We then discuss our methodology for forward modelling baseline and monitor seismic data sets, the computation of 4D seismic amplitudes attributes and our map extraction procedure.

4.1. Benchmark case UNISIM-I and the ensemble of models

Benchmark models commonly play an important role in testing methodologies for calibrating fluid-flow models. In this study, we validate our methodology using the synthetic UNISIM-I benchmark model (Avansi and Schiozer 2015b) consisting of the UNISIM-I-R reference model and a suite of derivative models. UNISIM-I-R is a fluid-flow model built in a high-resolution grid using publicly available data (e.g. core descriptions, well logs, 2D/3D seismic data) from the Namorado field, Campos Basin, Brazil. While the original structural interpretation is used to define the top and bottom reservoir surfaces and fault locations, sequential indicator simulation was used to model the facies distribution. The UNISIM-I-R performance evaluation accounts for small-scale heterogeneities distributed within these facies using a $[\Delta x, \Delta y, \Delta z] = [25, 25, 1]$ m grid-cell size discretised into a corner-point grid with $326 \times 234 \times 157$ active cells (approximately 3.4 million in total). The high level of detail offers both a reliable geological model and suitable derivative models for simulations that honour production history data. For a detailed description of the UNISIM-I-R model, we refer the reader to Avansi and Schiozer (2015b).

Figure 7 illustrates the processes applied to define the UNISIM-I-R suite of derivative models. Schiozer *et al* (2017) details the generation of an ensemble of 500 models that can be used to evaluate uncertainties in the initial stages of field production. This approach implies that each model in the ensemble is a potential reservoir scenario. It further describes the use of discretized Latin hypercube with geostatistics to identify reservoir uncertainties and define scenarios combining: (1) geostatistical realisations of facies, porosity, net-to-gross (NTG) and permeability (K); and (2) uncertainty parameters associated with rocks and fluids (e.g. water-oil-contact, relative permeability), production operations (e.g. well failures) and economic factors (e.g. oil price, costs). The authors also indicate that a subset of 100 models is sufficient for spanning the range of potential outcomes (Schiozer *et al* 2017).

Because flow-simulation modelling in high-resolution grids is a time-consuming process, the geological model reservoir properties (porosity, permeability, NTG) are up-scaled, which results in the UNISIM-I-H ensemble of 100 models (figure 7). The UNISIM-I-H reservoir models are built

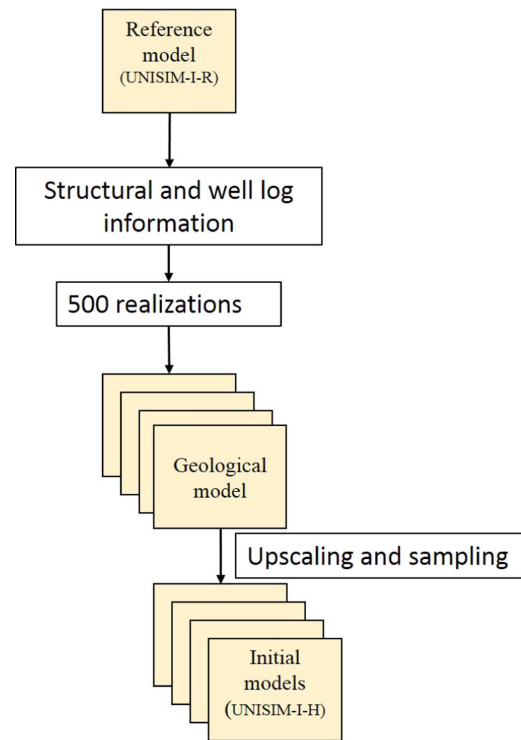


Figure 7. Diagram presents UNISIM-I-R derivative models. UNISIM-I-R provides structural and four vertical wells' information to generate 500 independent geostatistical realisations resulting in the ensemble of geological models. The 100 UNISIM-I-H initial models are specified after applying an upscaling and sampling procedure (Schiozer *et al* 2017).

for HM and uncertainty-reduction analyses in a post-development phase at date t_2 (31 May 2024). UNISIM-I-H has 11 years of production history (2013–24) based on the operation of four vertical, ten horizontal producers and 11 horizontal injectors (see figure 8) discretized into a $81 \times 58 \times 20$ corner-point grid (i, j, k -directions, respectively) with $[dx, dy, dz] = [100, 100, 8]$ m grid-cell size. We refer readers to Avansi and Schiozer (2015b) and Schiozer *et al* (2017) for further details on the uncertainty attributes considered when generating the ensemble.

4.2. Seismic forward modelling

Our 4D seismic workflow begins by applying a standard simulator-to-seismic workflow (Lumley 1995b, Lumley and Behrens 1998, Stephen and MacBeth 2006, Emerick and Rodrigues 2007, Hurren *et al* 2012) to model synthetic seismic amplitudes from each fluid-flow model in the ensemble. The workflow begins by extracting static (e.g. porosity, NTG) and dynamic (e.g. pressure, water saturation) properties and then applying Gassmann fluid substitution to estimate the P- and S-wave impedance volumes (Lumley 1995b, Mavko *et al* 2011). We use NTG estimates to infer the shale percentage within each grid cell (V_{Shale}). We note that increasing V_{Shale} values decreases 4D signal sensitivity to pressure and water saturation changes and therefore should be accounted for when estimating acoustic impedances associated with the static and dynamic response of fluid-flow

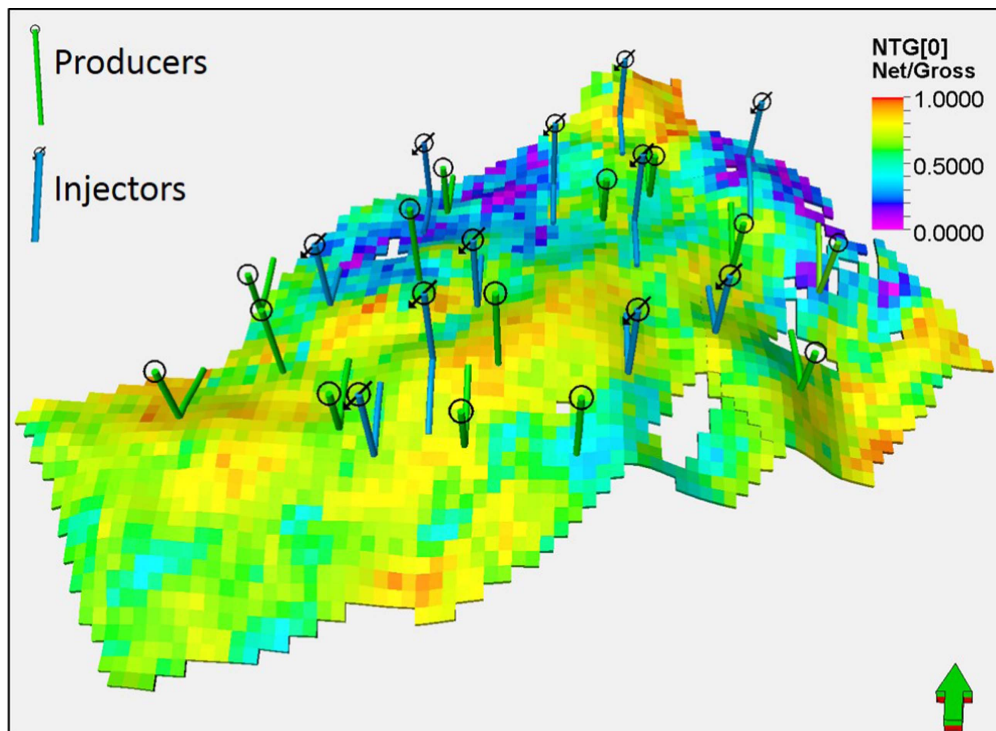


Figure 8. UNISIM-I-H: well pattern in the reservoir-top showing the positions of four vertical producers, ten horizontal producers and 11 injectors. Grid cells are colour coded by porosity.

models. We invoke the Hertz–Mindlin model to derive pressure sensitivity of dry bulk and shear moduli (Avseth *et al* 2011). While there are pressure sensitivity models that better predict rock pressure sensitivity (Saul and Lumley 2013, Saul *et al* 2013), it is beyond our scope to evaluate the application of these models on simulator-to-seismic workflows. Finally, we use Batzle and Wang (1992) relationships to model the fluid response to pressure and temperature.

We convert the fluid-flow model from depth to two-way travel time assuming an average background P-wave velocity ($V_p = 2.5 \text{ km s}^{-1}$) within all the simulation cells for both the baseline and monitor surveys. Because the procedure for time-to-depth conversion (i.e. constant, 1D or 3D velocity model) is likely very similar for both surveys, the effects of this choice have only a second-order effect in 4D seismic applications, since we are looking at relative—not absolute—model differences. We calculate RCs from computed P-wave acoustic impedances using a normal-incidence approximation (Telford *et al* 1990), and subsequently convolve these with a 50 Hz Ricker wavelet to generate synthetic 3D seismic amplitude volumes. We apply an identical modelling procedure to generate the monitor survey data. The choice of a 50 Hz wavelet frequency assumes that we are operating in a typical offshore reservoir in Brazil where modern marine seismic data quality is excellent and a 10–80 Hz spectrum is common (Ullmann De Brito *et al* 2010).

Having modelled the two seismic survey vintages, we can calculate any 4D amplitude attribute, representing the monitor-baseline difference. We elect to work in the amplitude domain as the errors associated with seismic inversion

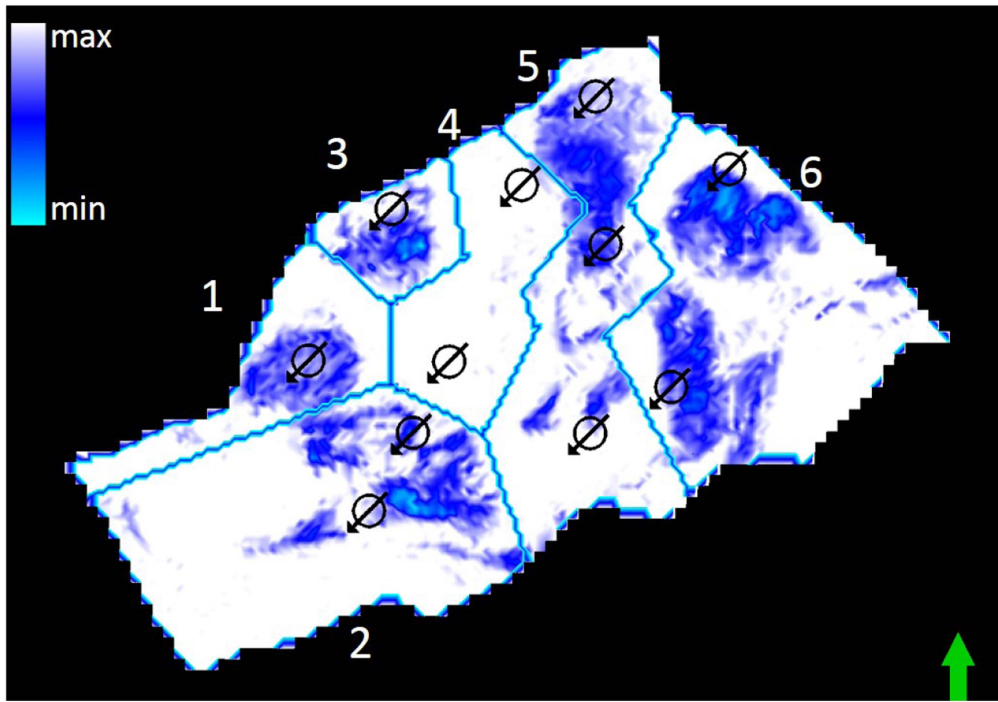
can lead to significant uncertainty in P- and S-wave impedance estimates (Lumley 2006, Landa and Kumar 2011, Souza *et al* 2017). We first extract independent maps of baseline and monitor by taking the rms of 4D seismic amplitudes over a specific time window around the horizon of interest. Finally, we derive a ΔA map by subtracting the baseline from a monitor 4D seismic amplitude rms map and calculating the ILDM attribute and the OF_S value used in the model classification procedure.

5. Results

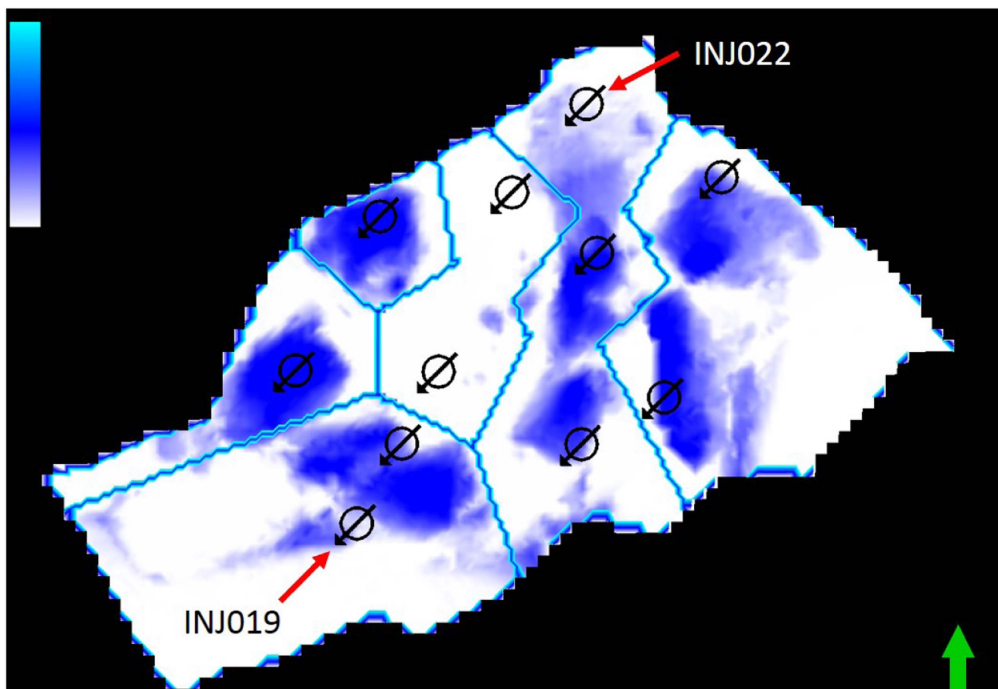
We present the results obtained by applying the described methodology for model classification and selection to the benchmark UNISIM-I-R and UNISIM-I-H models. We start by partitioning the reference 4D seismic amplitude map into different logical regions for interpretation. We then examine reservoir properties of the models to understand why certain models are classified as different model types (i.e. Types 1–4 discussed above).

5.1. Reservoir target and 4D seismic modelling

Figures 9(a) and (b) present the reference 4D seismic amplitude (ΔA) and water saturation change (ΔS_w) maps, respectively. The overall high visual correlation between these two maps suggests that 4D seismic amplitudes can be used as a ΔS_w proxy in this scenario (although pressure changes should also be considered in more general applications). Most of the reference 4D seismic amplitude change in



(a)



(b)

Figure 9. (a) 4D amplitude map superimposed with well injector locations; and (b) map of ΔS_w extracted from the reference model (UNISIM-I-R) at the same time interval used to generate the 4D amplitude map. Red arrows show the location of water injector wells that are unlikely to be interacting. Note that the 4D amplitudes are well correlated with the reference ΔS_w . Note that some map areas are not well correlated due to thin zones of water that the seismic data do not have the adequate resolution to image correctly.

figure 9(a) is visually correlated with the location of injector wells; however, closer examination suggests that some injectors are unlikely to be in communication (e.g. INJ019 and INJ022). Thus, with the aim of establishing linkages between water injection and local production in the fluid-movement trends, we partition this map into more locally

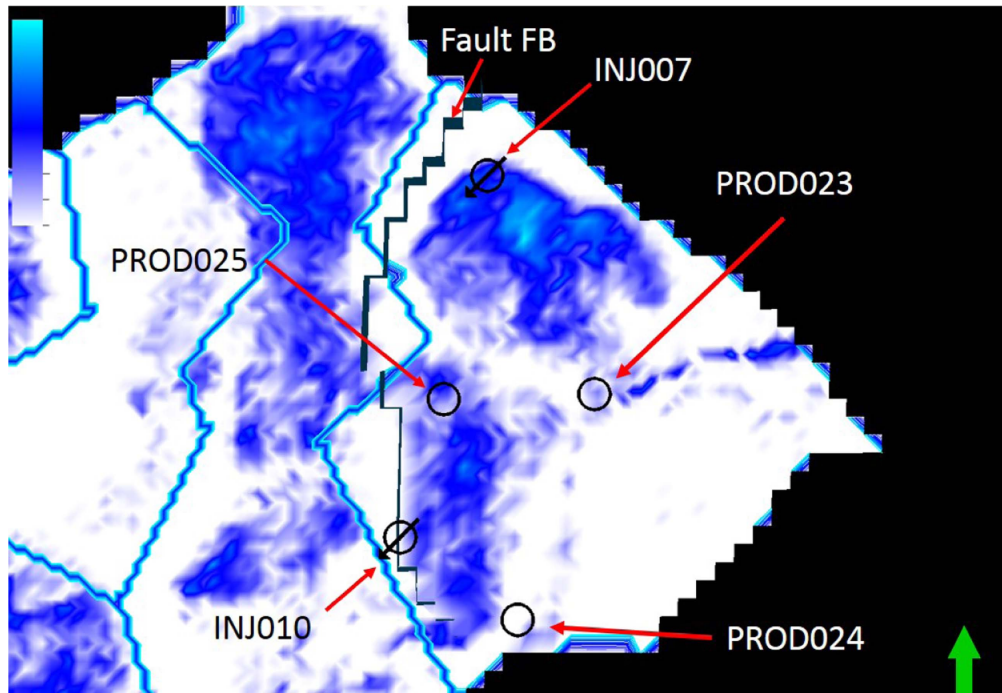


Figure 10. Boundaries of the region of interest from figure 9(a) highlighted in light blue on the 4D seismic amplitude map superimposed with three producers (PROD023, PROD024 and PROD025) and two injectors (INJ007 and INJ010).

autonomous regions based on the reference 4D amplitude map using Voronoi algorithm (Arthur and Vassilvitskii 2007) injector locations as centroids. The consistency between injector location and reference 4D signal within each region should improve our capability to investigate local causal relations and therefore establish conceptual correlations between reservoir properties and production behaviour.

Figure 10 shows the partitioned region of interest on which we focus during this investigation. This region contains three producer (PROD023, PROD024 and PROD025) and two injector (INJ007 and INJ010) wells, and is isolated from the rest of the reservoir by the known sealing fault, FB. INJ007 and INJ010 are completed in Layers 9 and 10 and commence water injection after approximately 2000 and 2200 days of production, respectively. The injection strategy focuses on sustaining reservoir pressure and thereby supporting the oil production rate. PROD023A is completed in Layer 8 and starts producing water after 3167 days of production (figure 11(b)). Note that the models in the ensemble predict a much earlier water breakthrough arrival time in comparison with production history, indicating that these models require further property updates in the vicinity of the well in order to delay the arrival of water. PROD024A is completed at Layer 2 and starts producing water after approximately 2600 days of production. Conversely to observations at PROD023A, the majority of the models in the ensemble predict water arrivals much later than expected, again highlighting the need for reservoir model updating. Finally, PROD025 completed at Layer 3 starts producing water after approximately 2500 days of production. The variation on these predictions highlights that this ensemble of models represent only an initial

attempt to model the correct reference model UNISIM-I-R response. Thus, our goal is to identify those models out of the full ensemble that are the most consistent with both seismic and production data that could form the basis of a subsequent round of fluid-flow reservoir model updating.

5.2. Methodology Application

To identify the source of the water produced by the wells in the region, we extract an rms map around Horizon 5 (top of Layer 5) of the reservoir (figure 10). The 4D signal in this region suggests that the water injected by INJ010 is likely to be moving towards PROD025. We note that the rms seismic amplitude map has a theoretical vertical resolution of approximately 12.5 m due to the 50 Hz Ricker wavelet and the 2.5 km s^{-1} velocity in the seismic forward modelling procedure. This explains why this map does not contain information related to the PROD023A completed in Layer 8, approximately 30 m below the map extraction window. The 4D seismic signal in the vicinity of PROD024 also suggests that the INJ010 is the source of the water produced at that well (figure 11(b)).

5.3. Model classification

To classify the models according to the methodology described above, we first calculate OF_S and OF_P and then apply the T_S and T_P thresholds. We use a value of $T_S = 0.44$ that is half of the OF_S range, while OF_P values within $T_P = \pm 300\%$ are deemed acceptable according to previous evaluations (Avansi *et al* 2016). To illustrate this, we show OF_P values per producer well in figure 12, where each

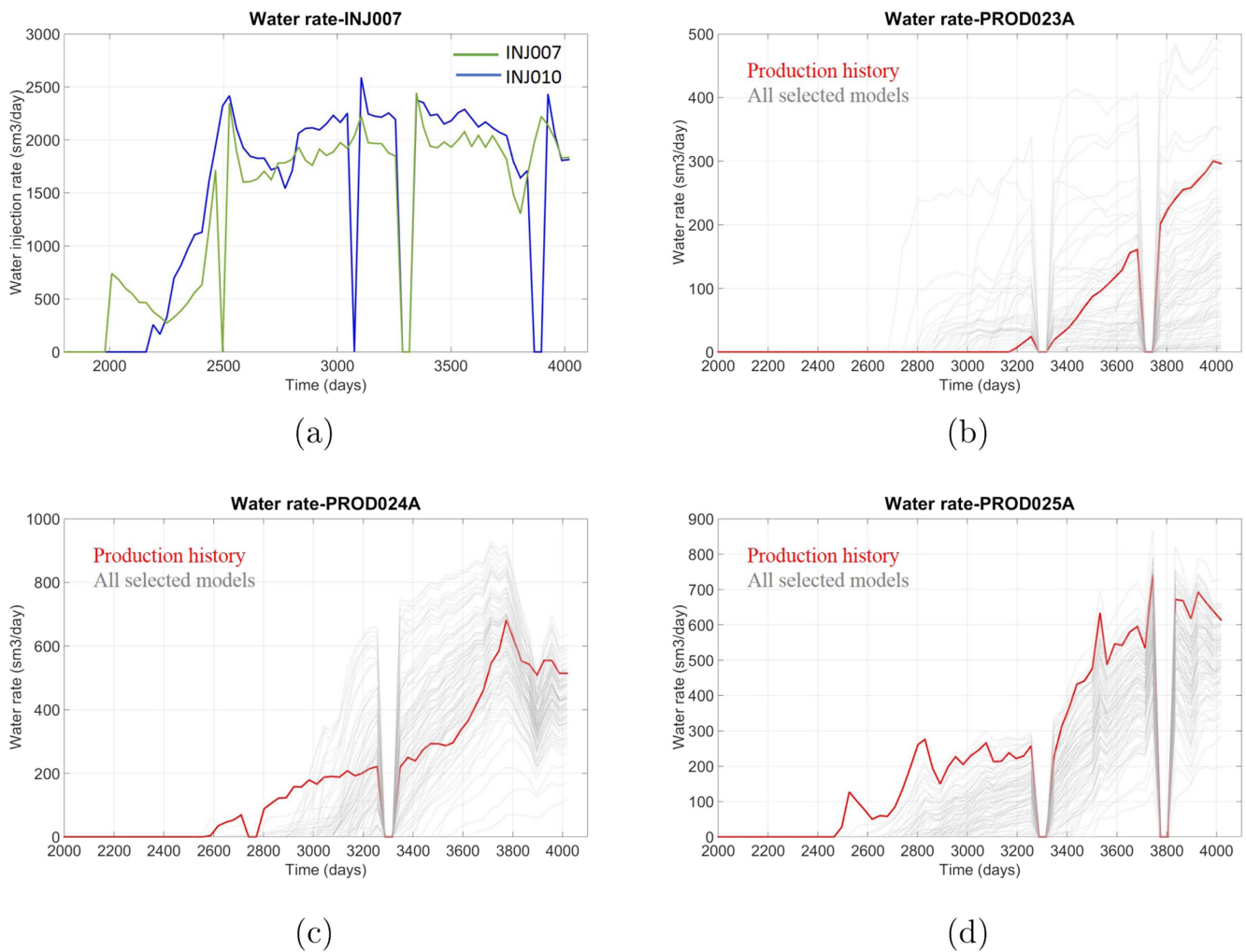


Figure 11. (a) Water injection rate of the wells INJ007 and INJ010 and water-rate production history (in red) superimposed with the flow-simulation response of the models in the ensemble for the producer wells: (b) PROD023; (c) PROD024A and (d) PROD025.

symbol represents a single model in the ensemble and the blue region indicates the models deemed acceptable based on our T_P criterion. While a 300% threshold may seem somewhat high, we stress that the ensemble of models require further updating, as they do not yet present high-quality matches (figures 11(a)–(c)). In fact, using a lower T_P would likely discard models broadly consistent with both seismic and production data.

By examining the 4D seismic amplitudes in figure 10, we identify two major 4D anomalies associated with INJ010 and INJ007. To quantitatively assess and classify the models, we estimate OF_S using the ILDM within the region of interest for the entire ensemble. Figure 13 shows a cross-plot of the OF_S and OF_P for Region 6 (see figure 9(a)) colour coded by type, where again each marker represents one model of the ensemble. This plot shows the classified model Types 1–4, as well as the four models (m_1 , m_2 , m_3 and m_4 , respectively) used as examples of Types 1–4 in the ensuing discussion (indicated by the red cross). When enforcing both seismic and production selection criteria, we classify nine Type 1, 49 Type 2, 11 Type 3 and 25 Type 4 models.

Figure 14(a)–(d) present the ILDMs of the four selected representative models. We observe that the quality of the match varies within the region. Note that the ILDMs have zero values at locations where the input attributes are well matched; thus, the area nearby INJ007 exhibits a better match than around INJ010. We also observe that the ILDMs for m_3 and m_4 show a poorer match than m_1 and m_2 between the reference and modelled amplitude maps, which is captured in figure 14 by the increase in OF_S from 0.28 (m_1) to 0.64 (m_4).

Figure 15(a) superimposes the simulated and production history of the water rate for Type 1 models. These models indeed provide a better match to the production history when compared to Type 2 and 4 models (Type 3 models also provide acceptable production match). Figure 15(b) shows the water-rate production curves for all models presented in figure 13 and highlights PROD025 OF_P values provided by the m_1 , m_2 , m_3 and m_4 models. Similar to the OF_S values, the computed OF_P values increase once the quality of the match between the production history and the simulated water rate deteriorates.

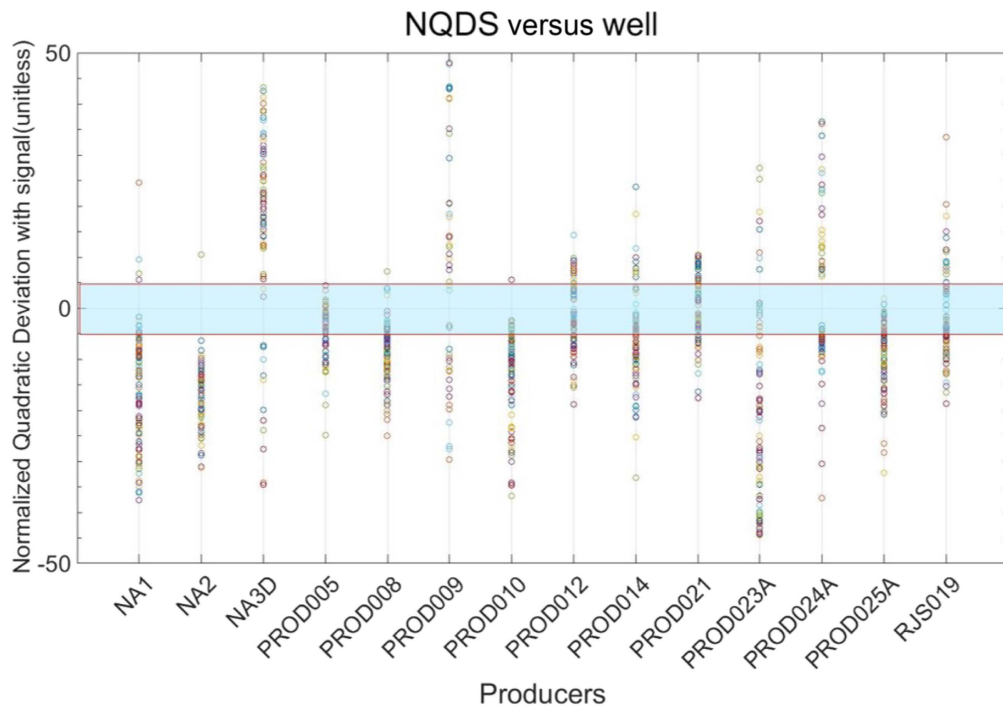


Figure 12. NQDS values for each producer well for the ensemble of models where each circle represents a different model. A model is selected as having an ‘acceptable’ production data fit if the OF_p value of any given model falls within the $\pm 300\%$ acceptance range highlighted in light blue.

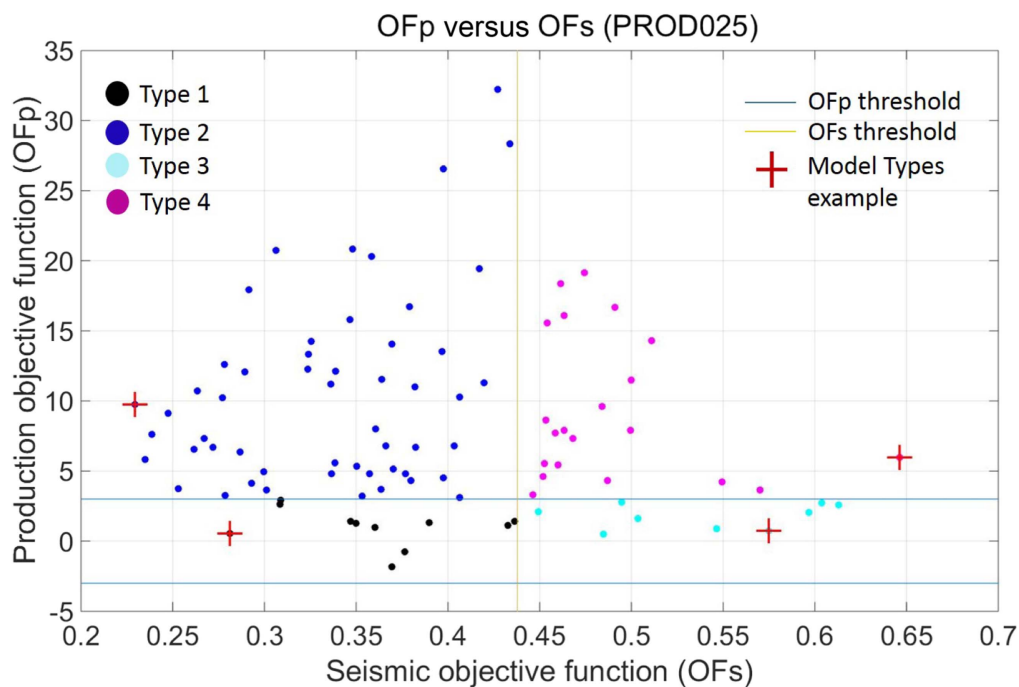


Figure 13. PROD025 production objective function (OF_p) versus seismic objective function (OF_s). Model Types 1–4 are colour coded in black, blue, cyan and purple, respectively. Note that m_1 , m_2 , m_3 and m_4 are highlighted in red.

5.4. Interpretation of model classification results

The model types indicate how well each model matches (or not) seismic and production data. We consider these insights as interpretation hypotheses that should be evaluated according to their consistency between seismic and production data. For example, figures 16(a)–(e) present the fluid-

flow ΔS_w distribution at the layer where PROD025 is completed for the reference model (UNISIM-I-R), $m_1 - m_4$, respectively. Both m_1 and m_2 present a reasonable visual agreement with the observed ΔS_w in the vicinity of the INJ007 (red arrow); however, there is a greater discrepancy between the modelled and reference ΔS_w in the INJ010 area

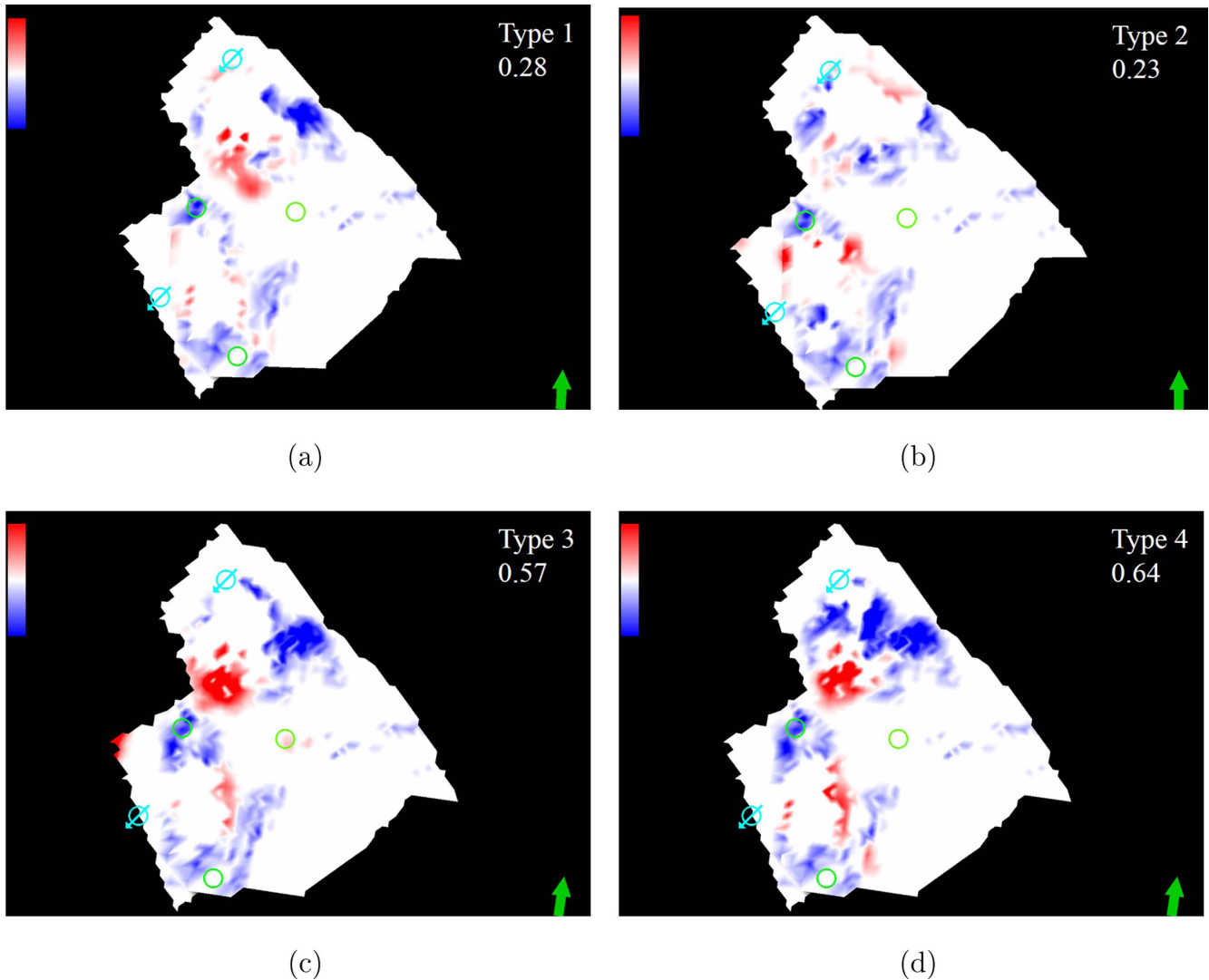


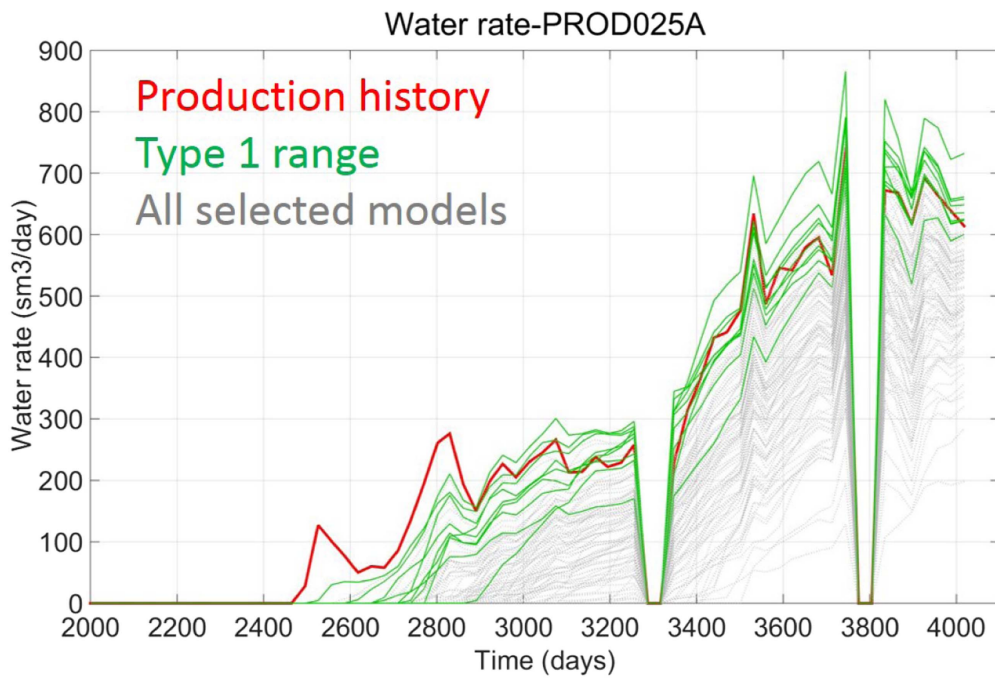
Figure 14. ILDM maps of the (a) m_1 , (b) m_2 , (c) m_3 and (d) m_4 and their correspondent OF_S values labelled in the upper right corner. Smaller OF_S values indicate a better match between the reference and synthetic 4D seismic amplitude maps. Injector and producer well locations are indicated in cyan and green, respectively. Note that the seismic acceptance threshold is 0.44.

(yellow arrow). Also note that more water has reached this area in m_1 , explaining why the PROD025 starts producing water before m_2 (figure 15(b)). Both the INJ007 and INJ010 areas in models m_3 and m_4 (figures 16(d) and (e)) poorly correlate with the reference ΔS_W in figure 16(a). Figures 17(a)–(e) show ΔS_W distributions for the true and $m_1 - m_4$ models, respectively. We present cross-sections to better highlight the INJ010 completion. Water moves vertically and sweeps the area in $m_1 - m_4$; however, we do not observe this trend in the true ΔS_W distribution (red arrow in figure 17(a)). This explains why there is a delay in the water arrival-time predictions made by these models (figures 15(a) and (b), respectively). The m_1 and m_2 ΔS_W distribution trends indicate the existence of high vertical permeability zones within the area. Also, the ΔS_W increase at the bottom layers of $m_1 - m_4$ is not confirmed by the true changes in water saturation.

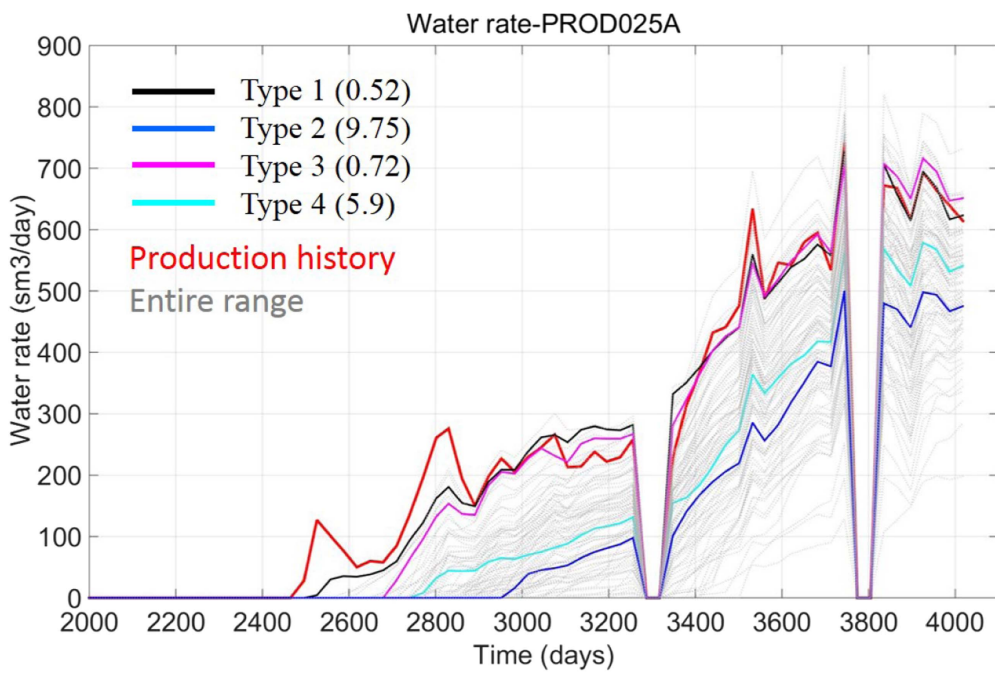
Figures 18(a)–(e) compare the ΔS_W distributions for the true and $m_1 - m_4$ models in the vicinity of the horizontal PROD025 completion, respectively. The water injected by

INJ010 reaches PROD025 in m_1 faster than in m_2 (see red arrow in figures 18(b) and (c)). We also note that the ΔS_W gradient between INJ007 and PROD025 is higher in m_1 than in m_2 , which explains why m_2 predicts water arrival 300 days later than expected (figure 15(b)). The layers in between the INJ007 and PROD025A completions are completely swept on model m_3 (in figure 18(d)). This pattern is also observed in the reference model (figure 18(a)), which explains why model PROD025A in m_3 fairly well predicts the history of the water production rate after 2900 days. ΔS_W below INJ007 layers in model m_4 is similar to the distribution on m_1 and m_4 , even though m_4 poorly predicts the water-rate production on PROD025 (figure 15(b)).

Figures 19(a)–(e) present cross-section comparison of the ΔS_W distributions between the true, $m_1 - m_4$ models for the horizontal INJ007 completion, respectively. Note the increase in ΔS_W in both models; however, the water sweeps the entire reservoir range in m_2 suggesting the presence of a high vertical permeability trend in the area (red arrow). We observe a similar, but less pronounced pattern in m_1 , which offers a



(a)

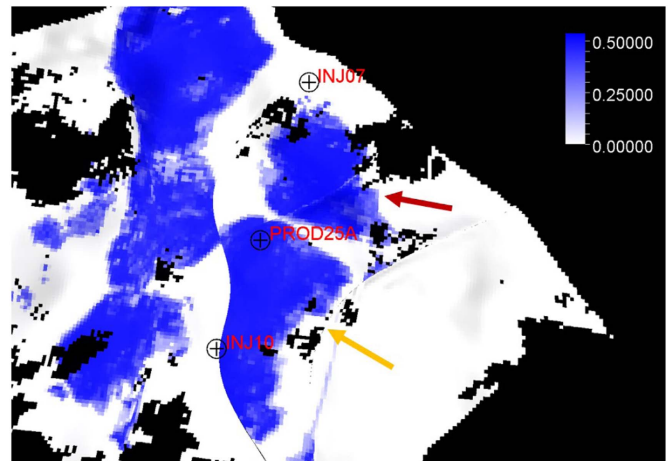


(b)

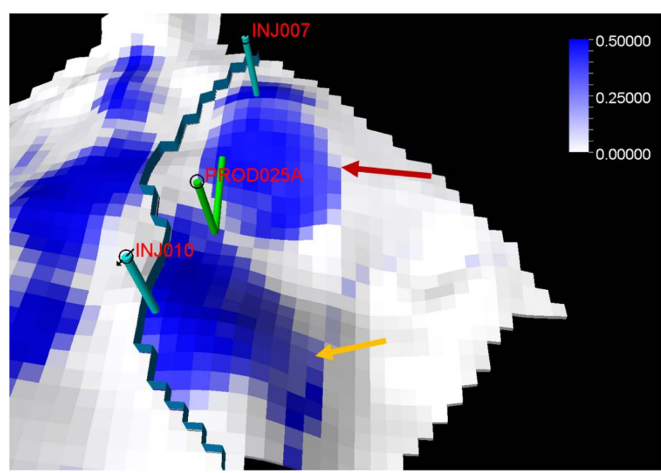
Figure 15. Observed (red) and simulated PROD025 water-rate curves from (a) Type 1 (in green) and Type 2–4 models (in grey); and (b) m_1 – m_4 .

better match with the true ΔS_w than m_2 . This further explains why m_2 has less accurate water-rate predictions as water moves to the bottom layers instead of towards the top layers (i.e. where PROD025 is completed). We observe that there is an agreement between ΔS_w at the bottom layers of the model m_3 and m_4 reference in figure 19(a).

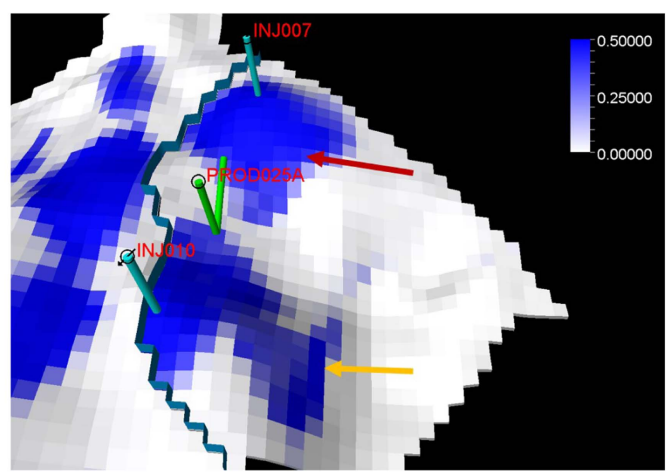
Overall, such analysis allows us to infer the presence (or absence) of permeability flow paths and barriers that could generate the observed ΔS_w trends. Thus, a closer examination of the permeability distributions of these models should provide additional details about the reservoir mechanisms in place.



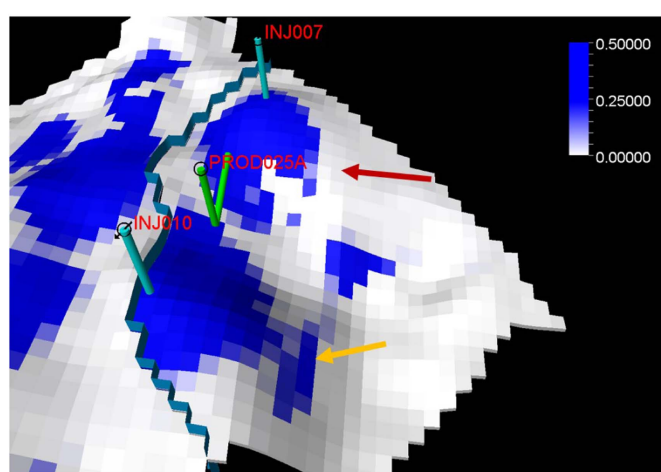
(a)



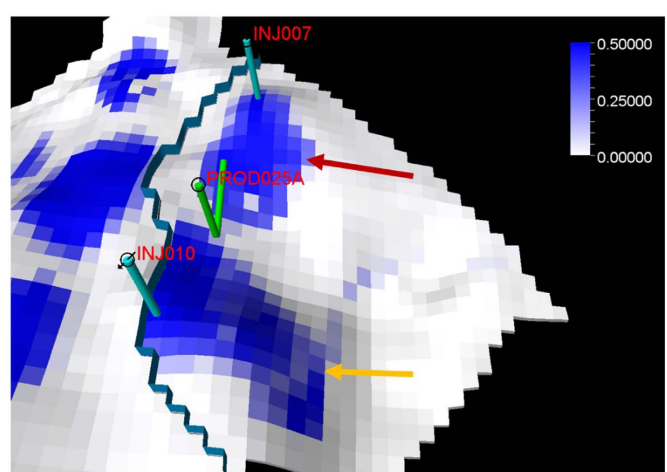
(b)



(c)



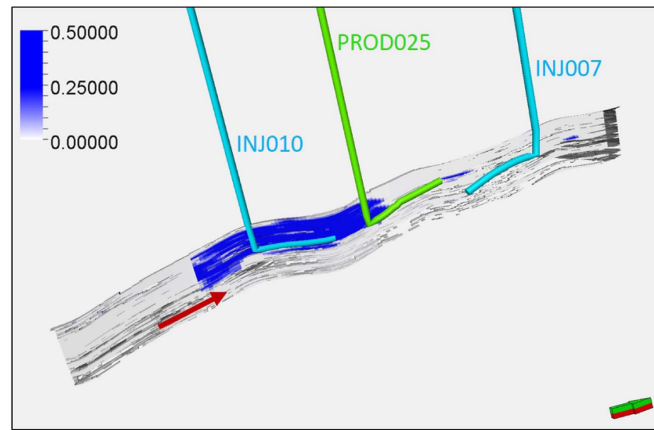
(d)



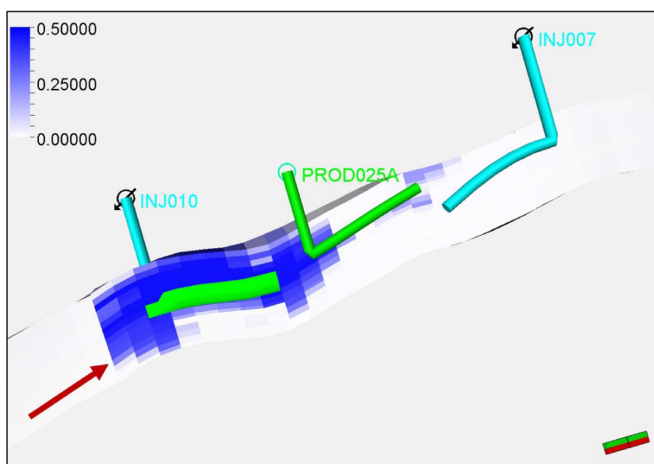
(e)

Figure 16. Water saturation distribution from the (a) true reference model (UNISIM-I-R); (b) m_1 ; (c) m_2 ; (d) m_3 ; and (e) m_4 fluid-flow models.

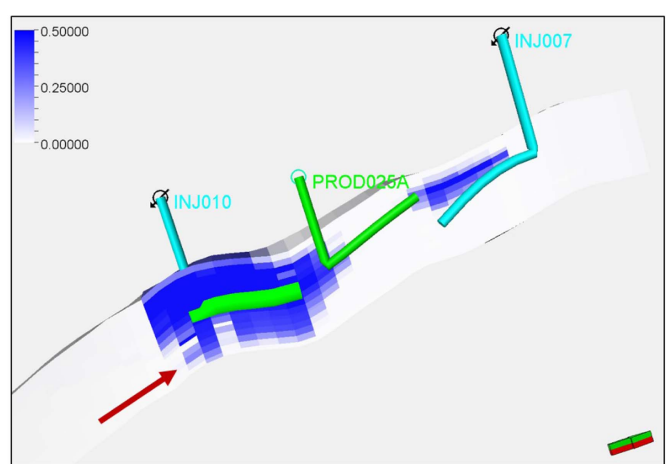
Downloaded from https://academic.oup.com/jge/article-abstract/15/4/1561/5204267 by BIBLIOTECA CENTRAL UNIV ESTADUAL CAMPINAS user on 21 July 2020



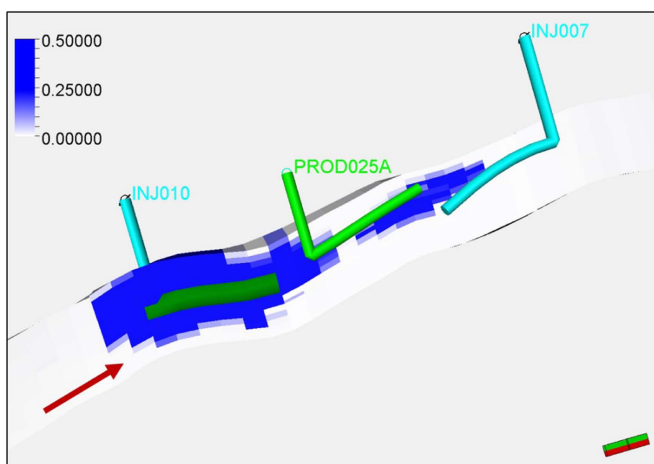
(a)



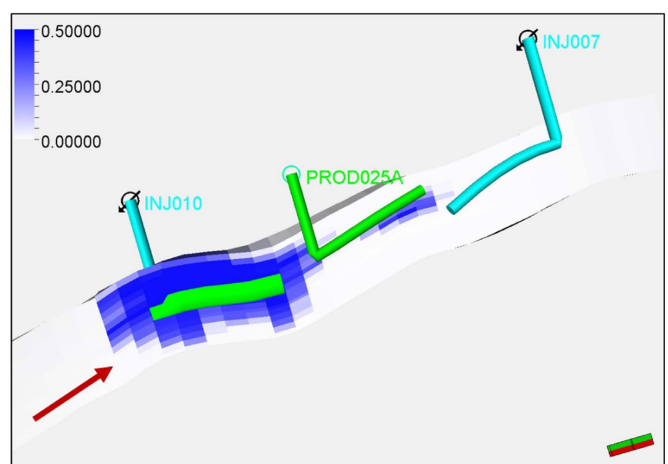
(b)



(c)

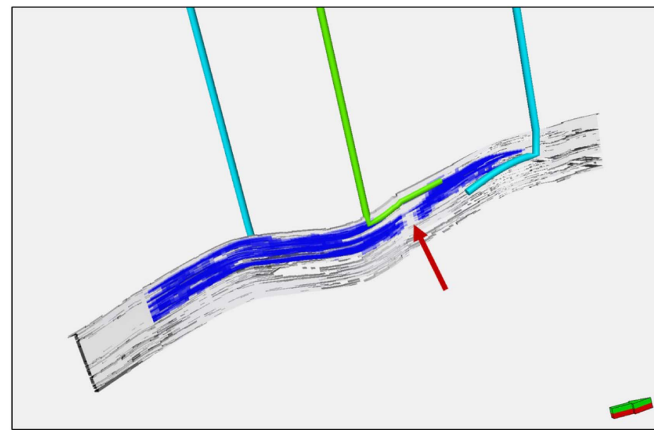


(d)

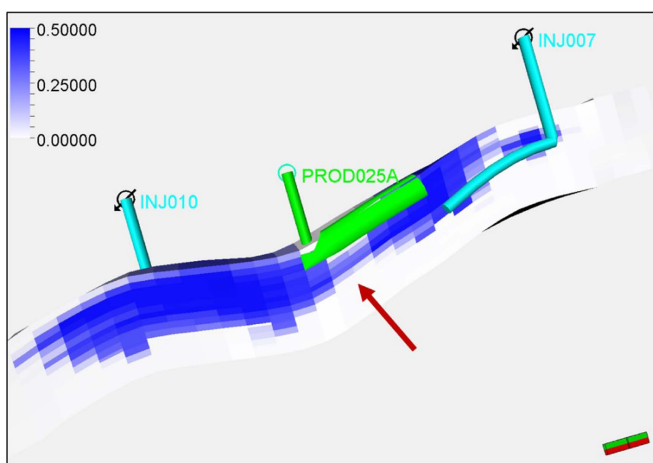


(e)

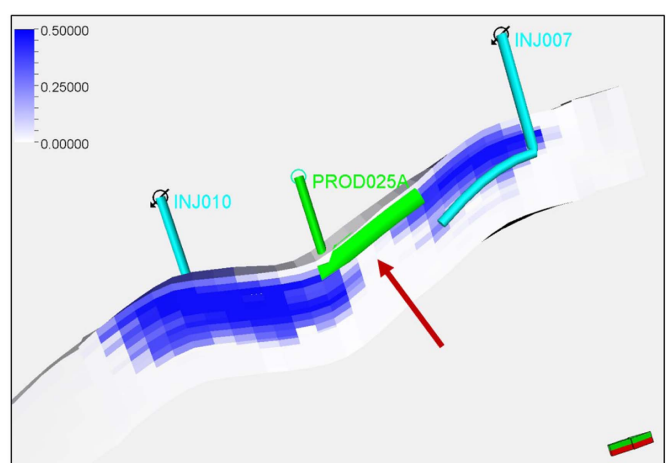
Figure 17. Comparison of the water saturation distribution of the (a) reference; (b) m_1 ; (c) m_2 ; (d) m_3 ; and (e) m_4 fluid-flow models highlighting the INJ010 completion.



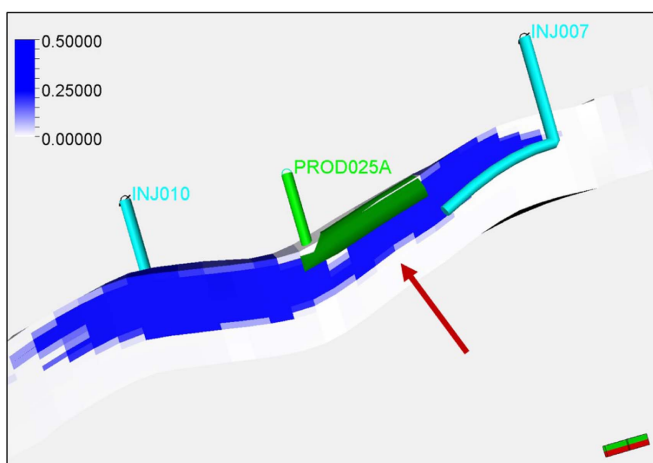
(a)



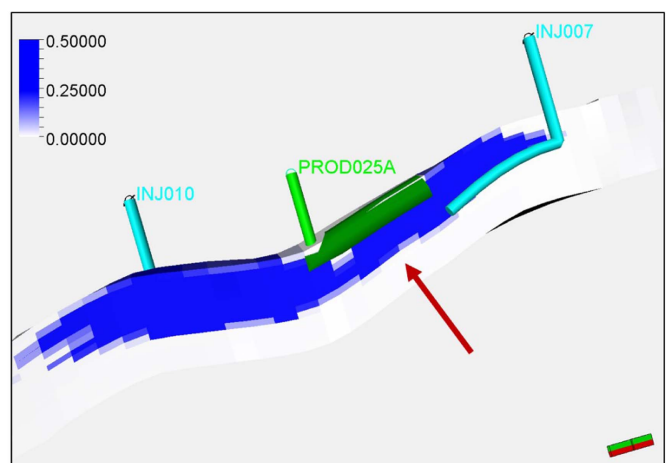
(b)



(c)

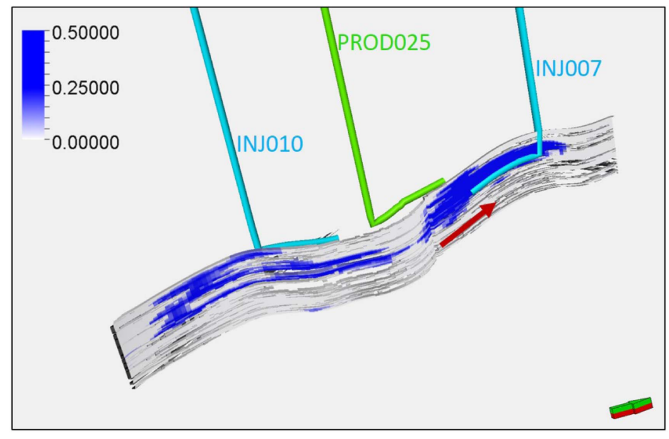


(d)

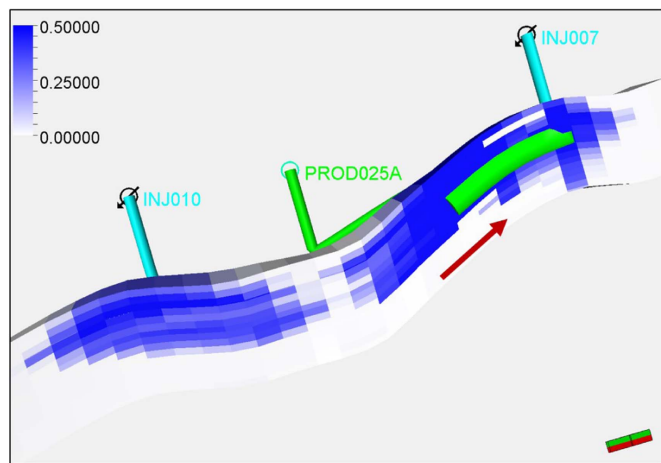


(e)

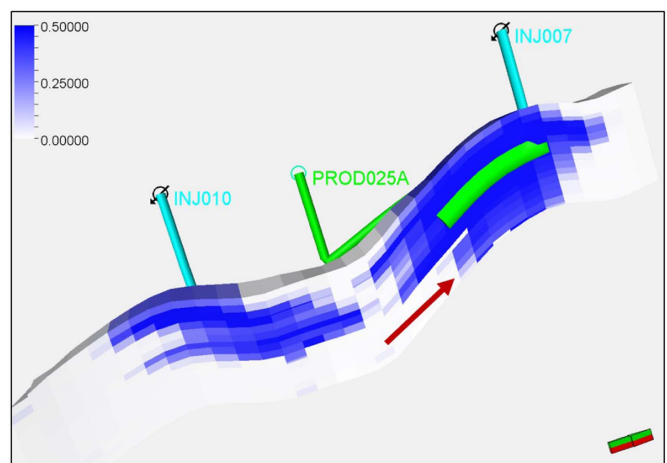
Figure 18. Comparison of the water saturation distribution of the (a) reference; (b) m_1 ; (c) m_2 ; (d) m_3 ; and (e) m_4 fluid-flow models highlighting the PROD025 completion.



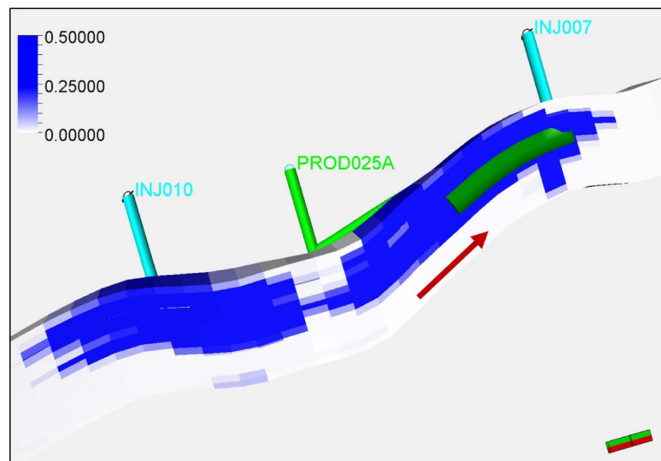
(a)



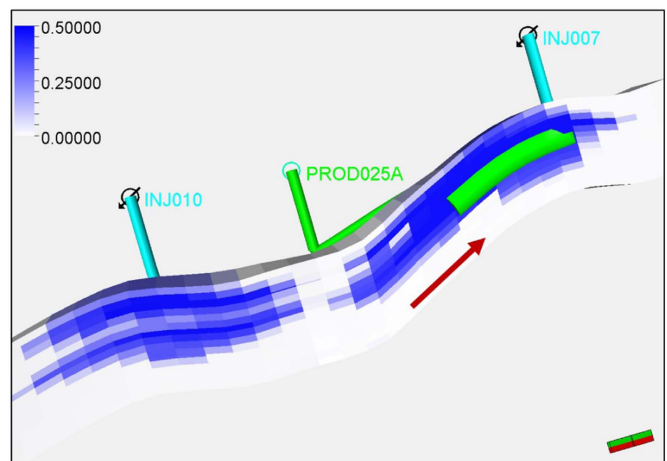
(b)



(c)



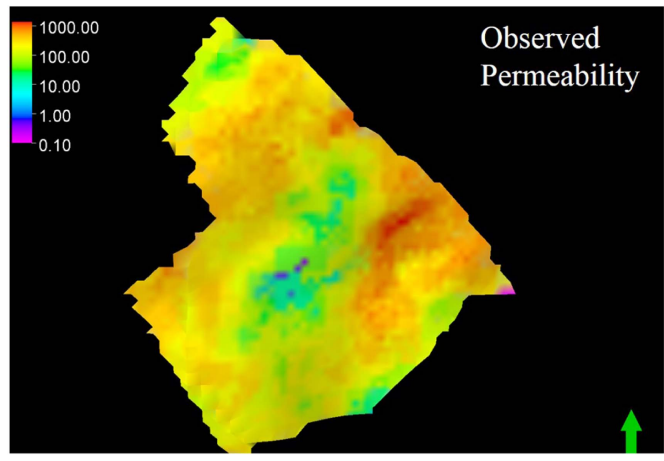
(d)



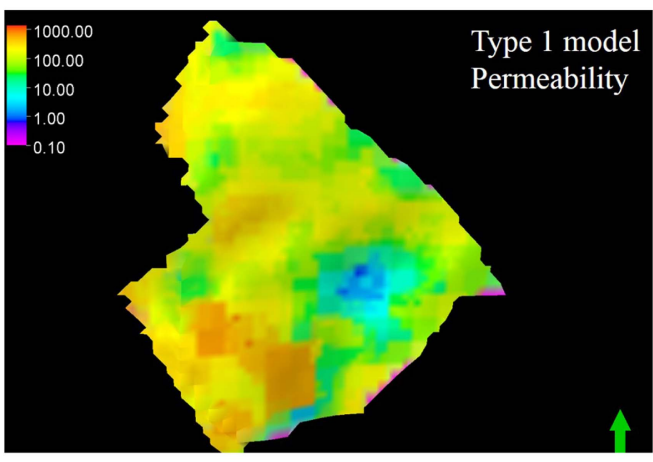
(e)

Figure 19. Comparison of the water saturation distribution of the (a) reference; (b) m_1 ; (c) m_2 ; (d) m_3 ; and (e) m_4 fluid-flow models highlighting the INJ007 completion.

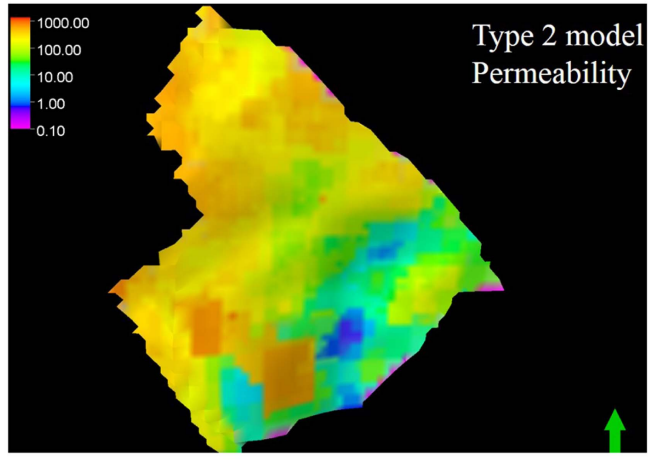
Downloaded from https://academic.oup.com/jge/article-abstract/15/4/1561/5204267 by BIBLIOTECA CENTRAL UNIV ESTADUAL CAMPINAS user on 21 July 2020



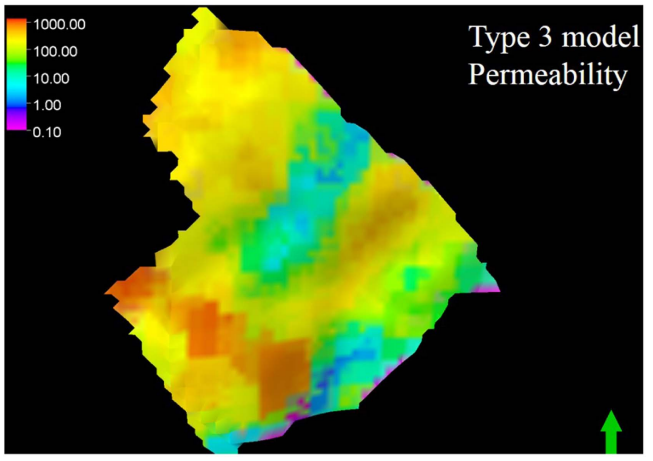
(a)



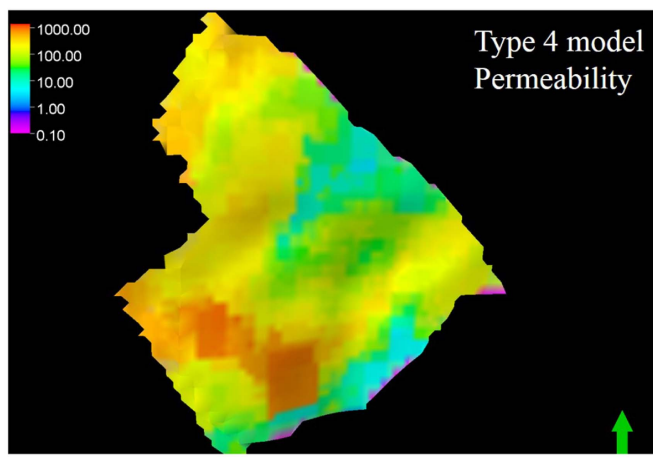
(b)



(c)



(d)



(e)

Figure 20. Rms map of the permeability distributions of the: (a) reference (UNISIM-I-R); (b) m_1 ; (c) m_2 ; (d) m_3 ; and (e) m_4 models. Maps are extracted at the same time/depth interval used for the rms map of the amplitude changes.

Downloaded from https://academic.oup.com/jge/article-abstract/15/4/1561/5204267 by BIBLIOTECA CENTRAL UNIV ESTADUAL CAMPINAS user on 21 July 2020

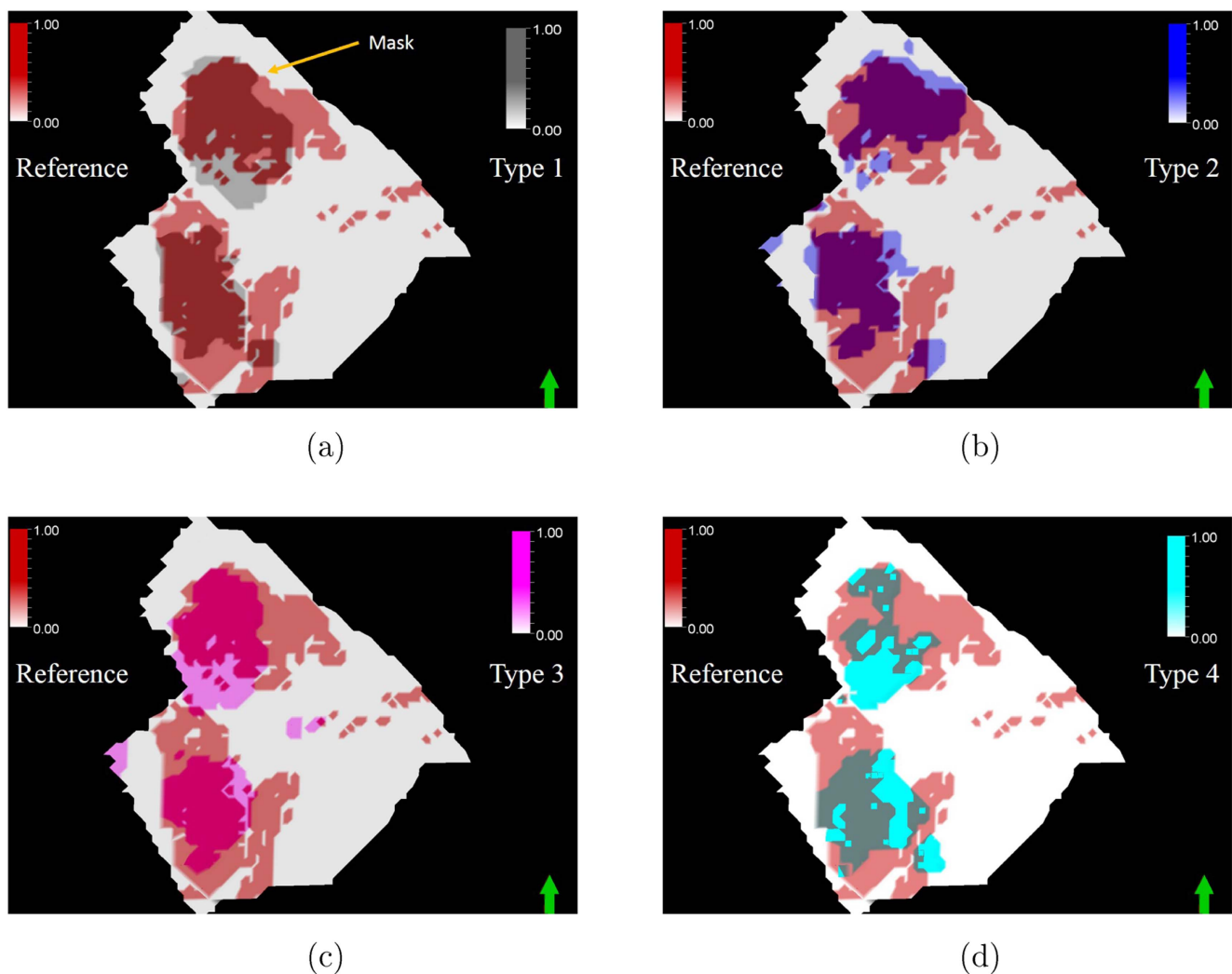


Figure 21. Superimposition of the binary images resulting from the reference (in red) amplitude changes with those resulting from synthetic seismic amplitude maps from (a) m_1 (in grey); (b) m_2 (in blue); (c) m_3 (in pink); and (d) m_4 (in cyan).

5.5. Permeability distribution interpretation

Figures 20(a)–(e) show the rms map (i.e. averaged to the seismic resolution) of the permeability distribution extracted from the UNISIM-I-R and $m_1 - m_4$ models, respectively. A qualitative comparison between these maps shows locations that correlate in magnitude and/or pattern with the true reference permeability distribution presented in figure 20(a). Note that models $m_1 - m_4$ offer reasonable visual matches at the north of the area of interest, while any correlation seems unlikely towards the south. All models contain a major permeability anomaly located at the south (figures 20(b)–(e)) added in earlier attempts to improve the match between simulated and observed production rates (figure 20(a)) (Mesquita *et al* 2015). As a result, the water injected by INJ010 moves southward along the high-permeability anomaly, decreasing the synthetic 4D seismic amplitudes in the area. The ILDM of all model types shows extended areas in blue in the region where the synthetic 4D rms map indicates an absence of 4D signal (figure 14). Furthermore, this high-permeability structure may be the cause of the delay in the predicted time of water arrival (figure 15) as the water

saturation front moves from INJ010 to the south instead of northeast towards PROD025.

In a quantitative interpretation of these permeability distributions, we should account for the fact that 4D seismic attributes only highlight the fluid-flow trends between two fixed moments in time. For instance, figure 10 highlights the presence of the known sealing fault FB. By inspecting this map, we infer the fault’s presence by observing a lack of 4D signal to the west of INJ010. However, this inference is only made possible because the water saturation front has reached the fault; otherwise, we would simply have insufficient information to do so.

To overcome this issue, we propose a quantitative interpretation of permeability maps based on the binary maps used to estimate the ILDM (figures 21(a)–(d)). We develop 4D permeability masks by subtracting the clusters of the reference and synthetic 4D seismic amplitude maps. Figures 21(a)–(d) show models $m_1 - m_4$, respectively. These are used as boundary masks for cross-plotting true versus modelled permeability distributions from model Types 1–4 (figures 20(a)–(d), respectively).

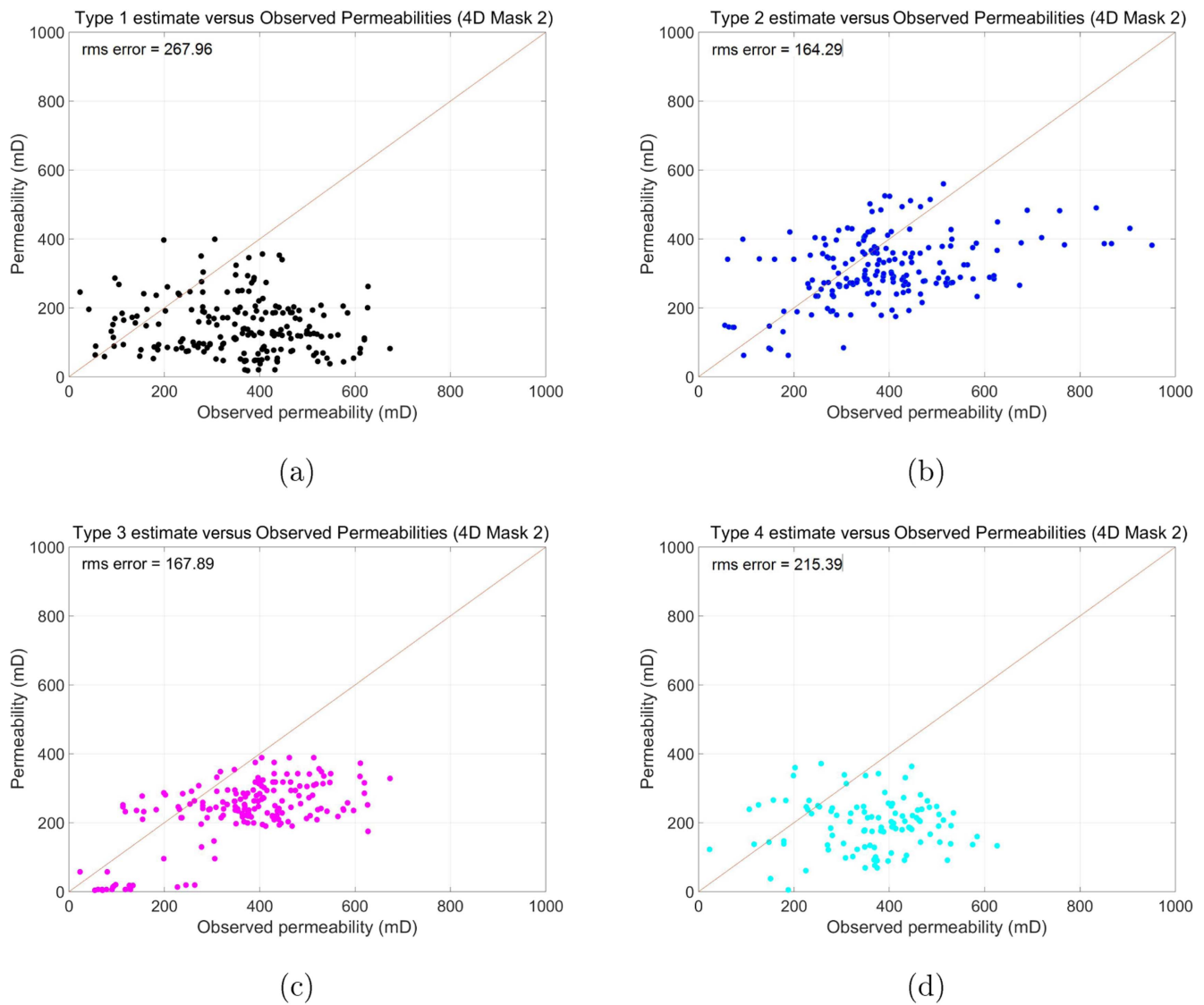


Figure 22. Cross-plots between the reference and modelled permeability distributions within \mathcal{M}_2 and their respective RMSE values (figure 21(a)) for (a) m_1 ; (b) m_2 ; (c) m_3 ; and (d) m_4 .

In our region of interest, we use the mask \mathcal{M} (figure 21(a)). In figures 22(a)–(d) we cross-plot model Types 1–4 versus the true permeability within region \mathcal{M} . This area, located to the north of our region of interest, presents a better visual match between the observed and modelled permeability distributions (figure 20) than the region in the vicinity of the INJ010 nearby the permeability anomaly. The m_1 and m_2 root-mean-square error (RMSE) are 267.96 and 164.29 mD, while the m_3 and m_4 are 167.89 and 215.39 mD (figure 22). Note that m_1 presents the highest error in relation to the other model types. The differences between the true and m_1 permeabilities within \mathcal{M} illustrate these higher errors. Rather than being the best, a Type 1 model indicates the optimal compromise between the quality of seismic and production data predictions as a function of T_S and T_P . Illustrating this further, in figure 13 we observe that m_2 has a lower OF_S than m_1 , which justifies the smaller error of the m_2 permeabilities; however, m_1 outperforms m_2 water-rate predictions at PROD025 (figure 15(b)), highlighting the impact

of the permeability distributions in deeper layers, where the extracted 4D seismic amplitude maps could not provide any information. Note that \mathcal{M} is located in the vicinity of the permeability anomaly in the fluid-flow models (figure 20) and therefore offers a less accurate match between the reference and modelled 4D seismic amplitudes.

6. Discussion

Our results indicate that the methodology developed above successfully categorises fluid-flow models in the ensemble according to their consistency with both 4D seismic and production data. By doing so, there are several resulting interpretation scenarios of potential fluid-flow paths and barriers. Our methodology improves the exchange of information between 4D amplitude maps, production data and static and dynamic reservoir properties. In this section, we discuss three issues that we view as important in the context

of applying this procedure on field data: (1) vertical resolution; (2) the advantages of model/map partitioning; and (3) permeability distribution analysis.

6.1. Vertical resolution considerations

Seismic vertical resolution should be taken into account when incorporating information extracted from 4D seismic maps into fluid-flow models. In our case, using a 50 Hz Ricker wavelet results in a theoretical vertical resolution of approximately 12.5 m. Because the UNISIM-I-H model builds in a grid with cells of dimensions $100 \times 100 \times 8 \text{ m}^3$, this means that our 4D amplitude maps will be unable to discriminate vertically varying information within less than $\pm 12.5 \text{ m}$ around the surface chosen to extract the map. In contrast, UNISIM-I-H has lateral and vertical permeability distributions for each of the 21 layers of 8 m thickness within the 161 m thick reservoir. Because 4D amplitude maps are extracted along Layer 5 using a $\pm 20 \text{ ms}$ time window, this implies that the observed hardening in the 4D amplitudes results from water saturation movements through the vertical and lateral permeability structures within the length-scale of vertical seismic resolution. In our case, INJ007 and INJ010 are both completed much deeper (Layers 9 and 10, respectively) than PROD025 (Layer 3). This means that the water moves up the dip once the injection starts and affects the water-rate production. Ultimately, this suggests that there are high vertical permeability structures allowing this fluid-movement trend. This illustrates how important vertical resolution is to the quantitative application of 4D seismic attribute maps into fluid-flow models. Reservoir thickness, injector and producer completion depths, seismic bandwidth and map extraction methodology all need to be equally taken into consideration for an effective integrated interpretation.

6.2. Map partitioning

The partitioning of 4D amplitude maps allows for more localised quantitative interpretation that leads to better correlations between 4D amplitude changes and well production data within the region. Ideally, map partitioning should be based on apparent causal relations between both 4D seismic amplitude signal and production patterns. There is also a compromise between the partitioned area and the OF_S accuracy. In smaller regions, the OF_S values better represent how well the modelled and observed maps match. For instance, an independent OF_S calculation in the vicinities of the INJ010 and INJ007 in model m_2 results is 0.44 and 0.13, respectively. This further illustrates that the ILDM effectively quantifies the match between observed and synthetic 4D amplitude changes. In our case, we choose the entire Region 6 because the water injected at the INJ007 affects the PROD025 water-rate production.

Because our model classification methodology is based on OF_S and OF_P values, we are able to analyse the goodness of fit not only between the simulated and observed water-rate curves, but between the property distributions nearby the producer locations. Thus, the localised permeability

distributions of the selected models can be used as starting models for iterative optimisation procedures for further reservoir property updates (e.g. HM).

6.3. 4D seismic and production data analysis for permeability distribution estimate

By categorising the fluid-flow models in the ensemble regarding their consistency between seismic and production data, our methodology offers a systematic approach to an often overwhelming task. Systematically and automatically analysing the different models by considering their (in)consistency with seismic and production data allows us to better understand water saturation movement trends within the reservoir and the permeability distribution.

When analysing rms maps of 4D seismic attributes, it is important to remember that 4D seismic amplitude maps offer a vertically limited 'snapshot' of the reservoir fluid distribution at the time of the monitor survey. This means that the estimated ΔS_w distribution at the top layers of the reservoir results from the up-dip water movement trend highlighted by the fluid-flow models. The m_1 and m_2 cross-sections showing ΔS_w emphasise the importance of combining the 4D seismic and production data (figures 17–20) as these models offer potential reservoir scenarios to explain ΔS_w trends that are unclear by interpreting the 4D seismic amplitude maps alone. Limitations concerning the seismic vertical resolution and localised well information require this integrated interpretation for completeness. For instance, the increased ΔS_w at the bottom layers underneath INJ010 explains why m_2 (figure 17(c)) shows a delay in the water arrival time, as the water goes down the dip instead of up the dip towards the PROD025. Similarly, the poor ILDM match in the vicinity of INJ010 indicates that the 4D seismic amplitude information does not comply with the permeability anomaly found in that area (figures 20(b)–(e)). In this scenario, we could confirm that there is no anomaly because we have the true permeability distribution; however, this is not the case in practice and it becomes invaluable to know where to add permeability trends within the fluid-flow model.

Our approach offers quantitative insights into the permeability distributions and, by applying 4D seismic techniques, avoids the uncertainties associated with estimating permeability based on the inversion of seismic attributes. Furthermore, by classifying and selecting models in the ensemble, we estimate permeability distributions that are consistent with both 4D seismic amplitude and production data that can be directly used as inputs in future simulation runs to streamline model calibration processes.

7. Conclusions

We present a new methodology combining 4D amplitude and production data to select a preferred subset of models out of an ensemble of equiprobable fluid-flow model realisations. We develop ILDMs that allow us to quantify differences between observed and modelled 4D seismic amplitude maps

in an independent seismic objective function. When combined with a standard production objective function, this leads to an automated and systematic methodology to classify fluid-flow model response and to provide insights into delays and advances in the predicted water arrival times at production wells. Classifying fluid-flow models by types with respect to their consistency with seismic and production data is viewed as a good integration approach that leads to estimates of fault locations and hydraulic and reservoir property distributions such as permeability and porosity. The cross-plot analysis shows that identified models can contain physically coherent permeability estimates and therefore validates our methodology for real data applications. By introducing a quantitative interpretation integrating 4D seismic attributes and fluid-flow models, this methodology offers a rapid and systematic approach for the time-consuming task of interpreting a large number of fluid-flow models.

Acknowledgments

We thank our colleagues at the UWA Centre for Energy Geoscience for discussions and insights that contributed toward the findings in this article. We acknowledge Dr Guilherme Avansi for his comments and assistance with the UNISIM-I reservoir model and fluid-flow data. We acknowledge Capes Foundation, the ASEG Research Foundation and the UWA:RM Consortium Sponsors for partial financial support of this research.

ORCID iDs

Rafael Souza  <https://orcid.org/0000-0003-2614-2376>

References

- Arthur D and Vassilvitskii S 2007 k -means++: the advantages of careful seeding *SODA 07: Proc. of the 18th Annual ACM-SIAM Symp. on Discrete Algorithms* pp 1027–35
- Avansi G D, Maschio C and Schiozer D J 2016 Simultaneous history-matching approach by use of reservoir-characterization and reservoir-simulation studies *SPE Reserv. Eval. Eng.* **19** 694–712
- Avansi G and Schiozer D 2015a A new approach to history matching using reservoir characterization and reservoir simulation integrated studies *Offshore Technology Conf.* (Society of Petroleum Engineers)
- Avansi G and Schiozer D 2015b UNISIM-I: synthetic model for reservoir development and management applications *Int. J. of Model. Simul. Pet. Ind.* **9** 21–30
- Avseth P, Mukerji T and Mavko G 2011 *Quantitative Seismic Interpretation* (New York: Cambridge University Press)
- Aziz K and Settari A 1979 *Petroleum Reservoir Simulation* (London: Chapman & Hall)
- Barkved O 2012 *Seismic Surveillance for Reservoir Delivery* (EAGE Publications)
- Batzle M and Wang Z 1992 Seismic properties of pore fluids *Geophysics* **57** 1396–408
- Baudrier E, Nicolier F, Millon G and Ruan S 2008 Binary-image comparison with local-dissimilarity quantification *Pattern Recognit.* **41** 1461–78
- Bertolini A and Schiozer D 2011 Influence of the objective function in the history matching process *J. Pet. Sci. Eng.* **78** 32–41
- Calvert R 2005 *Insights and Methods for 4D Reservoir Monitoring and Characterization (Distinguished Instructor Series)* (Society of Exploration Geophysicists and European Association of Geoscientists and Engineers) (<https://doi.org/10.1190/1.9781560801696>)
- Derfoul R, Da Veiga S, Gout C, Le Guyader C and Tillier E 2012 Image processing tools for better incorporation of 4D seismic data into reservoir models *J. Comput. Appl. Math.* **240** 111–22
- Doyen P 2007 *Seismic Reservoir Characterization: an Earth Modelling Perspective* (EAGE Publications)
- Emerick R and Rodrigues J P D 2007 History matching 4D seismic data with efficient gradient based methods *SPE Europec/EAGE Annual Conf. and Exhibition SPE* 107179
- Fanchi J R 2006 *Principles of Applied Reservoir Simulation* (Amsterdam: Elsevier)
- Gomez S et al 1999 Gradient-based history-matching with a global optimization method *SPE Annual Technical Conf. and Exhibition* (Society of Petroleum Engineers) SPE-56756-MS
- Gosselin O, Aanonsen S, Aavatsmark I and Cominelli A 2003 History matching using time-lapse seismic (HUTS) *SPE Annual and Technical Conf.* (Society of Petroleum Engineers) SPE 84464
- Hurren C, Broad C, Duncan G, Hill R and Lumley D 2012 Successful application of 4D seismic in the Stybarrow Field, Western Australia *SPE Asia Pacific Oil and Gas Conf. and Exhibition* (Society of Petroleum Engineers) SPE 158753
- Huttenlocher D P, Klanderman G A and Rucklidge W J 1993 Comparing images using the Hausdorff distance *IEEE Trans. Pattern Anal. Mach. Intell.* **15** 850–63
- Kjelstadli R, Lane H, Johnson D, Barkved O, Buer K and Kristiansen T 2005 Quantitative history match of 4D seismic response and production data in the Valhall Field *Offshore Europe* (Society of Petroleum Engineers) SPE 96317
- Landa J and Kumar D 2011 Joint inversion of 4D seismic and production data *SPE Annual and Technical Conf.* (Society of Petroleum Engineers) SPE 146771
- Lumley D 2001 Time lapse seismic reservoir monitoring *Geophysics* **66** 50–3
- Lumley D and Behrens R 1998 Practical issues of 4D seismic reservoir monitoring: what an engineer needs to know *SPE Reserv. Eval. Eng.* **1** 528–38
- Lumley D E 1995a 4-D seismic monitoring of an active steamflood *SEG Technical Program Expanded Abstracts* (Society of Exploration Geophysicists) pp 203–6
- Lumley D E 1995b Seismic Time-Lapse Monitoring of Subsurface Fluid Flow *PhD Thesis* Stanford University
- Lumley D E 2006 Nonlinear uncertainty analysis in reservoir seismic modeling and inverse problems *SEG Technical Program and Expanded Abstracts* (Society of Exploration Geophysicists)
- Maschio C, Avansi G, Schiozer D and Santos A 2015 UNISIM report: study case for reservoir exploitation strategy selection based on UNISIM-I field *Technical Report* (<https://unisim.cepetro.unicamp.br/benchmarks/files/UNISIM-I-D.pdf>)
- Maschio C and Schiozer D J 2016 Probabilistic history matching using discrete Latin hypercube sampling and nonparametric density estimation *J. Pet. Sci. Eng.* **147** 98–115
- Matheron G 1975 *Random Sets and Integral Geometry* (New York: Wiley)
- Mavko G, Mukerji T and Dvorkin J 2011 *The Rock Physics Handbook* (Cambridge: Cambridge University Press)
- Meira L A A, Coelho G P, Santos A A S and Schiozer D J 2016 Selection of representative models for decision analysis under uncertainty *Comput. Geosci.* **88** 67–82

- Mesquita F B, Davolio A and Schiozer D 2015 A systematic approach to uncertainty reduction with a probabilistic and multi-objective history matching *Europec/EAGE Conf. and Exhibition (Madrid, Spain)* SPE 174359
- Obidegwu D 2015 Seismic Assisted History Matching Using Binary Image Matching *PhD Thesis* Heriott-Watt University
- Oliver D, Reynolds A and Liu N 2008 *Inverse Theory for Petroleum Reservoir Characterization and History Matching* (Cambridge: Cambridge University Press)
- Oliver D S and Chen Y 2011 Recent progress on reservoir history matching: a review *Comput. Geosci.* **15** 185–221
- Roggero F, Ding D, Berthet P, Lerat O, Cap J and Schreiber P 2007 Matching of production history and 4D seismic data—application to the Girassol Field, offshore Angola *SPE Annual and Technical Conf.* (Society of Petroleum Engineers) SPE 109929
- Saul M, Lumley D and Shragge J 2013 Modeling the pressure sensitivity of uncemented sediments using a modified grain contact theory: Incorporating grain relaxation and porosity effects *Geophysics* **78** D327–38
- Saul M J and Lumley D E 2013 A new velocity pressure compaction model for uncemented sediments *Geophys. J. Int.* **193** 905
- Schiozer D J, Avansi G D and Santos A A 2017 Risk quantification combining geostatistical realizations and discretized Latin hypercube *J. Braz. Soc. Mech. Sci. Eng.* **39** 575–87
- Schiozer D J, Ligerio E L, Suslick S B, Costa A P A and Santos J A M 2004 Use of representative models in the integration of risk analysis and production strategy definition *J. Pet. Sci. Eng.* **44** 131–41
- Schiozer D J, Santos A A d S d and Drumond P S 2015 Integrated model based decision analysis in twelve steps applied to petroleum fields development and management *Europec/EAGE Conf. and Exhibition* SPE 174370
- Souza R, Lumley D and Shragge J 2017 Estimation of reservoir fluid saturation from seismic data: amplitude analysis and impedance inversion as a function of noise *J. Geophys. Eng.* **14** 51–68
- Stephen K D and MacBeth C 2006 Inverting for the petro-elastic model via seismic history matching *SEG Annual Meeting*
- Telford W, Geldard L and Sheriff R 1990 *Applied Geophysics* 2nd edn (Cambridge: Cambridge University Press)
- Tillier E, Da Veiga S and Derfoul R 2012 Appropriate formulation of the objective function for the history matching of seismic attributes *Comput. Geosci.* **51** 64–73
- Tillier M L R and Veiga S D 2012 Simultaneous inversion of production data and seismic attributes: application to a synthetic SAGD produced field case *Oil Gas Sci. Technol.—Rev. IFP Energies Nouvelles* **67** 289–301
- Ullmann D, Brito D, Caletti L and de Moraes R 2011 Incorporation of 4D seismic in the re-construction and history matching of Marlim Sul deep water field flow simulation model *SPE Europec/EAGE Annual Conf. and Exhibition* SPE 143048
- Ullmann De Brito D, Moraes R and Emerick A 2010 The Marlim Field: incorporating time-lapse seismic in the assisted history matching *Proc. of SPE Latin American and Caribbean Petroleum Engineering Conf.* (Society of Petroleum Engineers)